Monthly Notices
of the
ROYAL ASTRONOMICAL SOCIETY

MNRAS **451,** 3587–3605 (2015) doi:10.1093/mnras/stv1129

Feeding versus feedback in active galactic nuclei from near-infrared integral field spectroscopy – X. NGC 5929

Rogemar A. Riffel,[1,2]★ Thaisa Storchi-Bergmann[2] and Rogério Riffel[2]

[1]*Departamento de Física, Centro de Ciências Naturais e Exatas, Universidade Federal de Santa Maria, 97105-900, Santa Maria, RS, Brazil*
[2]*Departamento de Astronomia, Instituto de Física, Universidade Federal do Rio Grande do Sul, CP 15051, 91501-970, Porto Alegre, RS, Brazil*

Accepted 2015 May 15. Received 2015 April 16; in original form 2015 January 16

ABSTRACT

We present near-infrared emission-line flux distributions, excitation and kinematics, as well as stellar kinematics, of the inner 520 × 520 pc^2 of the Seyfert 2 galaxy NGC 5929. The observations were performed with Gemini's Near-Infrared Integral Field Spectrograph (NIFS) at a spatial resolution of ∼20 pc and spectral resolution of 40 km s^{-1} in the J and K_1 bands. The flux distributions of H_2, [Fe II], [P II] and H recombination lines are extended over most of the field of view, with the highest intensity levels observed along PA = 60/240°, and well correlated with the radio emission. The H_2 and [Fe II] line emission originated in thermal processes, mainly due to heating of the gas by X-rays from the central active galactic nucleus (AGN). The contribution of shocks due to the radio jet is observed at locations co-spatial with the radio hotspots at 0.50 arcsec north-east and 0.60 arcsec south-west of the nucleus, as evidenced by the emission-line ratio and gas kinematics. The stellar kinematics shows rotation with an amplitude at 250 pc from the nucleus of ∼200 km s^{-1} after correcting for the inferred inclination of 18.3°. The stellar velocity dispersion obtained from the integrated K-band spectrum is $\sigma_* = 133 \pm 8$ km s^{-1}, which implies a mass for the supermassive black hole of $M_\bullet = 5.2^{1.6}_{-1.2} \times 10^7$ M$_\odot$, using the $M_\bullet$–σ_* relation. The gas kinematics present three components: (1) gas in the plane of the galaxy in counter-rotation relative to the stars; (2) an outflow perpendicular to the radio jet that seems to be due to an equatorial AGN outflow; and (3) turbulence of the gas observed in association with the radio hotspots, supporting an interaction of the radio jet with the gas of the disc. We estimated the masses of ionized gas and warm molecular gas to be ∼1.3 × 10^6 M$_\odot$ and ∼470 M$_\odot$, respectively.

Key words: galaxies: individual (NGC 5929) – galaxies: ISM – galaxies: Seyfert – infrared: galaxies.

1 INTRODUCTION

Detailed mapping of the gas distribution, excitation and kinematics around active galactic nuclei (AGNs) is fundamental to the understanding of the physics behind the AGN feeding and feedback processes. Near-infrared (IR) integral field spectroscopy (IFS) on 8–10-m telescopes of nearby galaxies has become a powerful tool for understanding these processes better, as it provides two-dimensional coverage with spatial resolution of a few to tens of parsecs at a spectral resolution that allows us to resolve the gas kinematics and permits isolation of the inflows and outflows in the central kiloparsec, where the relevant processes occur (e.g., Riffel et al. 2008; Müller-Sánchez et al. 2009; Davies et al. 2009; Storchi-Bergmann et al. 2010; Schartmann et al. 2010; Riffel & Storchi-Bergmann 2011a; Riffel, Storchi-Bergmann & Winge 2013b; Davies et al. 2014; Riffel, Storchi-Bergmann & Riffel 2014b).

Some of the main results obtained from IFS of the inner kiloparsec of active galaxies are:

(i) Ionized gas and molecular gas have distinct flux distributions and kinematics. The near-IR line emission at these scales originates from the heating and ionization of the gas by the AGN radiation and shocks produced by radio jets (e.g., Riffel et al. 2006; Riffel, Storchi-Bergmann & Nagar 2010a; Riffel et al. 2013b). The molecular H_2 emitting gas is usually more restricted to the plane of galaxies, with kinematics dominated by rotation and inflows in the disc in most cases. The ionized gas emission traces a more disturbed medium, usually associated with outflows from the AGN, but frequently showing also a rotation component from the disc of the galaxy (e.g., Riffel et al. 2010a; Riffel & Storchi-Bergmann 2011a,b; Storchi-Bergmann et al. 2010; Iserlohe et al. 2013; Mazzalay et al. 2014).

★ E-mail: rogemar@ufsm.br

(ii) Outflows are seen within hollow cones or from compact structures with mass outflow rates in the range 10^{-2}–10^{1} $M_{\odot}$ yr^{-1} for low-luminosity Seyfert and low-ionization nuclear emission-line region (LINER) galaxies (e.g., Riffel et al. 2009; Schönel et al. 2014) and 10^{2}–10^{3} $M_{\odot}$ yr^{-1} for high-luminosity Seyferts (e.g., McElroy et al. 2015). The outflows are observed with velocities from 200 to 800 km s^{-1} in ionized gas (Storchi-Bergmann 2013) and ∼150 km s^{-1} in H_2 when present (Davies et al. 2014).

(iii) Inflows are observed in H_2 (e.g., Müller-Sánchez et al. 2006; Riffel et al. 2013b; Mazzalay et al. 2014) in Seyfert galaxies and in low-ionization gas in LINERs (Fathi et al. 2006; Storchi-Bergmann et al. 2007; Schnorr-Müller al. 2011, 2014a,b) with mass inflow rates in the range 10^{-1}–10^{1} $M_{\odot}$ yr^{-1} (Storchi-Bergmann 2013, 2014).

(iv) The stellar kinematics of Seyfert galaxies reveals cold nuclear structures composed of young stars, usually associated with a significant gas reservoir (Riffel et al. 2010b, 2011c; Storchi-Bergmann et al. 2012; Hicks et al. 2013).

NGC 5929 is a spiral galaxy with a Seyfert 2 nucleus located at a distance of 35.9 Mpc.[1] NGC 5929 has a companion, NGC 5930 at 20 arcsec north-east from it (Page 1952). It presents a well-defined bipolar radio jet oriented along the position angle PA ≈ 60°, showing a triple structure with two bright hotspots, one located at 0.5 arcsec north-east from the nucleus and the other at 0.6 arcsec south-west from it. The third and fainter radio structure is observed at the nucleus of the galaxy (Ulvestad & Wilson 1984; Wilson & Keel 1989; Su et al. 1996). The orientation of the major axis of the large-scale disc is PA ≈ 45° (e.g., Schmitt et al. 1997).

The gas kinematics of NGC 5929 has been studied for at least three decades. Using long-slit spectroscopy along the orientation of the radio jet, Keel (1985) concluded that the ionized gas kinematics is consistent with rotation in the galaxy disc. Whittle et al. (1986) obtained long-slit spectra along PA = 60° and PA = −30° covering the H β and [O III] emission lines and found double-component emission-line profiles along PA = −30°. They suggested that the origin of these profiles was the superposition of the two components observed along PA = 60° (one in blue shift to the north-east and one in red shift to the south-west) and unresolved by their observations, at a seeing of 1.6 arcsec. Rosario et al. (2010) reported the detection of shocked gas associated with the north-east radio hotspot by comparing optical long-slit spectra obtained with the *Hubble Space Telescope* (*HST*) Imaging Spectrograph (STIS) with radio images. These authors found that the low-ionization gas (traced by H β emission) shows broader emission-line profiles than the high-ionization gas (traced by the [O III] λ5007 emission line) at locations near the radio hotspot and suggested that this broadening is due to the interaction of the radio jet with the narrow-line region (NLR). Evidence of shocks is also observed at the location of the south-western radio hotspot, for which Ferruit et al. (1999) showed that shock models with velocities of ∼300 km s^{1} are able to reproduce the optical and ultraviolet (UV) emission-line ratios. The low spectral and spatial resolutions and/or small spatial coverage of the data have not allowed the studies above to reveal the complete scenario for the gas kinematics in the nuclear region of NGC 5929, which we have been able to do now with our NIFS observations.

In Riffel et al. (2014b, hereafter called Paper I), we reported the discovery of a peculiar structure along PA = −30/150° in this galaxy from these observations, where the emission lines present double components. This structure was interpreted as being due to the interaction of the acquired gas from the companion with an equatorial outflow from the accretion disc around the central supermassive black hole (SMBH). In the present paper, we present a more complete study of the overall gas kinematics, as well as of the gas excitation and stellar kinematics of the inner 520 × 520 pc^2 of NGC 5929.

NGC 5929 is the 10th galaxy in a series observed by our group AGNIFS (AGN Integral Field Spectroscopy) in which we present the emission-line flux distributions and kinematics as well as the stellar kinematics of the inner few hundreds of parsecs of nearby active galaxies. The previous papers of this series have presented similar studies as this of the following galaxies:

I. ESO 428-G14 (Riffel et al. 2006)
II. NGC 4051 (Riffel et al. 2008)
III. NGC 7582 (Riffel et al. 2009)
IV. NGC 4151 (Storchi-Bergmann et al. 2009, 2010)
V. Mrk 1066 (Riffel et al. 2010a,b; Riffel & Storchi-Bergmann 2011a)
VI. Mrk 1157 (Riffel & Storchi-Bergmann 2011b; Riffel et al. 2011c)
VII. Mrk 79 (Riffel et al. 2013b)
VIII. NGC 1068 (Riffel et al. 2014a; Storchi-Bergmann et al. 2012; Barbosa et al. 2014)
IX. Mrk 766 (Schönel et al. 2014)

This paper is organized as follows. In Section 2 we describe the observations and data reduction. In Section 3 we present the results for the continuum and line emission, including line-ratio maps as well as the gas and stellar kinematics. The discussion of the results is presented in Section 4 and the conclusions are presented in Section 5.

2 OBSERVATIONS AND DATA REDUCTION

NGC 5929 was observed using the Gemini Near-infrared Integral Field Spectrograph (NIFS – McGregor et al. 2003) on the Gemini North telescope operating with the adaptive optics module ALTAIR on the nights of 2011 March 16, May 24 and June 16, under the observation programme GN-2011A-Q-43. The observations covered the J and K_l spectral bands, resulting in a wavelength coverage from 1.14 to 1.36 μm and 2.10 to 2.54 μm, respectively. The total on-source exposure time for each band was 6000 s and the observations were split into 10 individual on-source exposures plus five sky exposures for each band.

The data reduction followed standard procedures and was accomplished using tasks contained in the NIFS.GEMINI package, which is part of the IRAF software. The procedures included trimming the images, flat-fielding, sky subtraction, wavelength and s-distortion calibrations, remotion of the telluric absorption and flux calibration by interpolating a blackbody function to the spectrum of the telluric standard star.

The final data cubes contain ∼4500 spectra at an angular sampling of 0.05 arcsec × 0.05 arcsec, covering the inner 3 arcsec × 3 arcsec (520 × 520 pc^2) of NGC 5929. The angular resolution is 0.12 arcsec for both bands (corresponding to ∼20 pc at the galaxy), as obtained from the full width at half-maximum (FWHM) of the images of the telluric standard stars. From the FWHM of the emission-line profiles of Ar lamps, we obtain spectral resolutions of 1.7 Å for the J band and 3.2 Å for the K band, corresponding to a velocity resolution of ∼40 km s^{-1} for both bands.

In the top-left panel of Fig. 1, we present a large-scale R-band image of NGC 5929 and its companion NGC 5930 from

[1] As quoted in NASA/IPAC Extragalactic Database (http://ned.ipac.caltech.edu/).

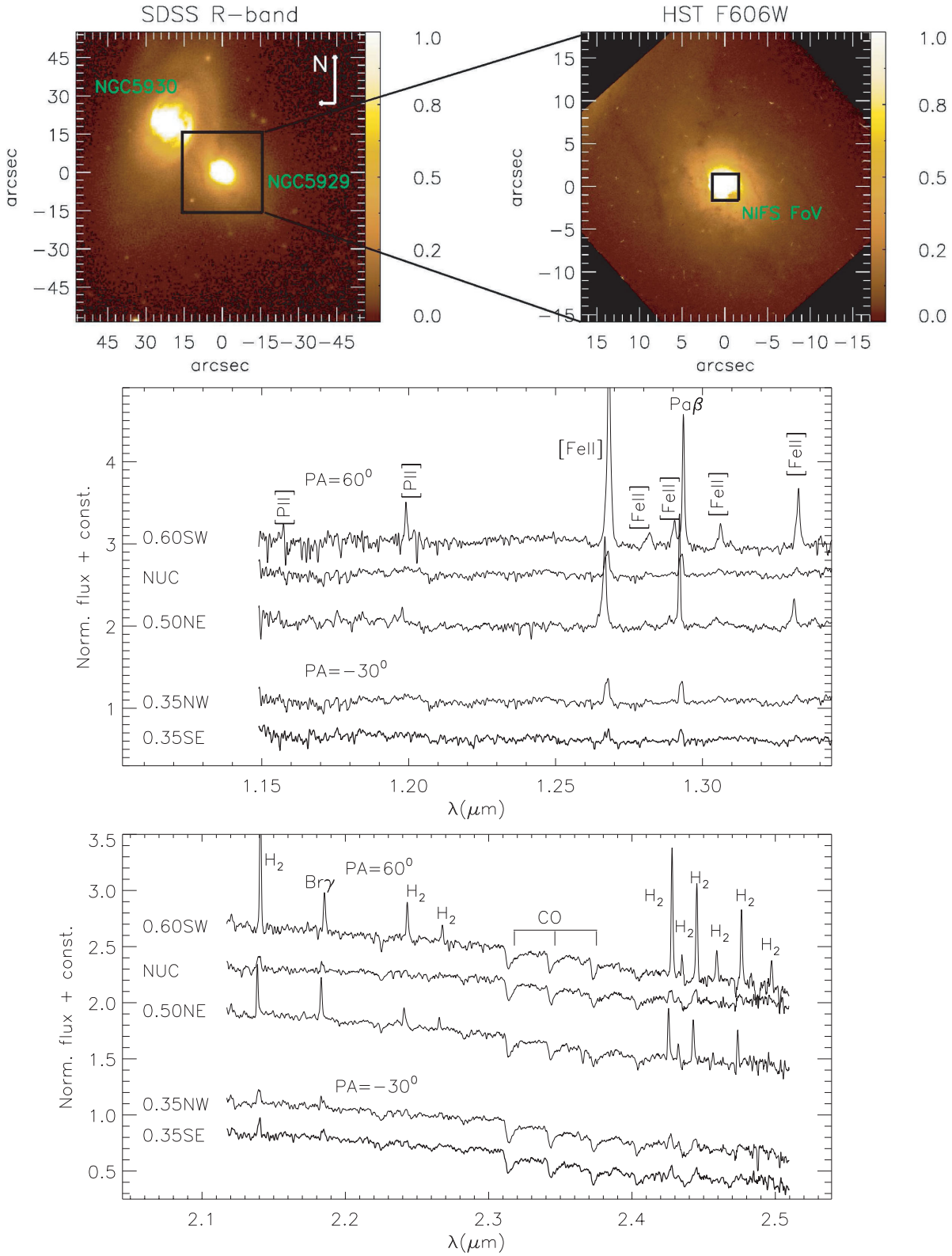

Figure 1. Top left: Large-scale image of NGC 5929 and NGC 5930 obtained in the *R* band from SDSS DR4 (Baillard et al. 2011). Top right: Optical image of the inner 30 arcsec × 30 arcsec of NGC 5929 obtained with the *HST* WFPC2 through the filter F606W (Malkan, Gorjian & Tam 1998), with the NIFS field of view represented by the green box. Middle: NIFS *J*-band sample spectra for the central region of NGC 5929, with the main emission lines identified. Bottom: NIFS *K*-band sample spectra for the central region of NGC 5929 with the main emission/absorption lines identified. The spectra shown were integrated within an aperture of 0.25 arcsec × 0.25 arcsec and the positions selected correspond to the south-western radio hotspot (0.60 arcsec SW of the nucleus), the nucleus (NUC) and the north-eastern radio hotspot (0.50 arcsec NE), plus two positions along PA = −30° (0.35 arcsec NW and 0.35 arcsec SE), along the peculiar outflow reported in Paper I.

the Sloan Digital Sky Survey, covering 1.5 arcmin × 1.5 arcmin (Baillard et al. 2011). The top-right panel shows an optical image of NGC 5929 obtained with the *HST* Wide Field Planetary Camera 2 (WFPC2) through the broad-band filter F606W from Malkan et al. (1998), covering the inner 30 arcsec × 30 arcsec. The green box represents the field of view of our NIFS data. The middle panel shows sample spectra obtained from the NIFS *J*-band data cube within apertures of 0.05 arcsec × 0.05 arcsec for the following positions (from top to bottom): 0.6 arcsec south-west of the nucleus, corresponding to the position of the south-western radio hotspot (Ulvestad & Wilson 1989); 0.5 arcsec north-east of the nucleus, corresponding to the position of the north-eastern radio hotspot (Ulvestad & Wilson 1989); the nucleus; 0.35 arcsec north-west and 0.35 arcsec south-east of the nucleus along PA = −30°, perpendicular to the radio jet, where we found that the emission lines present double components (Riffel et al. 2014b). The following emission lines are identified in the *J*-band spectra: [P II] λ1.14713 μm, [P II] λ1.18861 μm, [Fe II] λ1.25702 μm, [Fe II] λ1.27069 μm, [Fe II] λ1.27912 μm, H I Pa β λ1.28216 μm, [Fe II] λ1.29462 μm and [Fe II] λ1.32092 μm. The bottom panel of Fig. 1 shows the spectra in the *K* band at the same positions of those in the *J* band. We identified the H I Br γ λ2.16612 μm emission line and the H_2 emission lines at 2.12183, 2.15420, 2.22344, 2.24776, 2.40847, 2.41367, 2.42180, 2.43697 and 2.45485 μm. The CO absorption band-heads at ∼2.3 μm used to measure the stellar kinematics are also identified in the *K*-band spectra.

3 RESULTS

3.1 Emission-line profiles

As discussed in Paper I, the emission lines present double components along a strip (hereafter identified as the south-east to north-west or SE-NW strip) crossing the nucleus at PA = −30°, which has been attributed to gas outflowing from the nucleus perpendicular to the radio jet. In Fig. 2, we show a sample of the emission-line profiles of [Fe II] λ1.2570, H_2 λ2.1218 and Pa β from three locations:

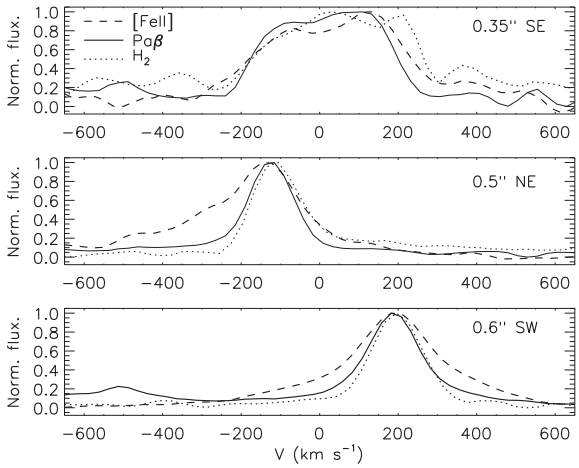

Figure 2. Sample of the [Fe II] λ1.2570, H_2 λ2.1218 and Pa β emission-line profiles at three locations: 0.35 arcsec south-east of the nucleus, along the SE-NW strip at PA = −30° (top panel); 0.50 arcsec north-east of the nucleus, at the position of a radio hotspot (middle panel); and 0.60 arcsec south-west of the nucleus, at the position of the other radio hotspot (bottom panel). The Pa β line profile is shown as a continuous line, the H_2 line profile as a dotted line and the [Fe II] emission-line profile as a dashed line.

along the SE-NW strip at 0.35 arcsec south-east of the nucleus (top panel) and at the positions of the radio knots along PA = 60° at 0.50 arcsec north-east (middle panel) and at 0.60 arcsec south-west (bottom panel) of the nucleus. The double components, reported in Paper I, are evident at the position 0.35 arcsec south-east, not only for [Fe II] but also for the other emission lines, with profiles presenting similar widths. Indeed, all emission lines detected along the SE-NW strip present similar double components. At the positions of the radio hotspots or knots, the [Fe II] profile is the broadest, H_2 is the narrowest and Pa β is between the two. H_2 and Pa β are well reproduced by a single Gaussian curve, while the [Fe II] profile clearly shows the presence of more than one component. A blue wing in the [Fe II] profile is observed for the position at 0.50 arcsec north-east of the nucleus. At 0.60 arcsec south-west of the nucleus, its profile is broader than a Gaussian curve. At positions away from the strip at PA = −30° and distant from the radio knots, the emission lines are well reproduced by a single Gaussian component, as discussed in Paper I.

As shown in Fig. 1, several emission lines are observed in the *J*- and *K*-band spectra of NGC 5929. To measure the emission-line flux distributions, we fitted the observed line profiles at each spatial position by Gaussian curves using the PROFIT routine (Riffel 2010). In Table 1, we present the measured fluxes for the emission lines within an aperture of 0.35 arcsec × 0.35 arcsec at five positions: the locations of the radio hotspots, at 0.50 arcsec north-east and 0.60 arcsec south-west of the nucleus; the nucleus; and at 0.35 arcsec south-east and 0.35 arcsec north-west of the nucleus along the strip at PA = −30° (the region where the equatorial outflow was observed in Paper I). Values followed by * were obtained from the sum of the fluxes of the two components. The [Fe II] λ1.2570 line profile was fitted by three Gaussian curves at 0.60 arcsec south-east of the nucleus (at the location of a radio hotspot), and the flux quoted in the table is the sum of the fluxes of the three components. Sample fits of the [Fe II] profile are shown in Paper I.

3.2 Emission-line flux distributions

To obtain the flux distributions, we fitted only one Gaussian to all emission lines, for simplicity. Although two or three components reproduce the profiles better at some locations, as discussed above, the resulting error in the fluxes at these locations is lower than 5 per cent.

Fig. 3 shows the flux distributions for all measured emission lines. In each panel, black represents masked regions where the flux values are smaller than the standard deviation of the continuum values near the emission line or the uncertainty in the flux is higher than 40 per cent. Light grey contours delimit the masked regions and the green contours overlaid on some panels are from the radio image of Ulvestad & Wilson (1989). At most locations, the uncertainties in flux are smaller than 15 per cent. For illustration, we have rebinned the spaxels to 1/3 of their original size and then interpolated their fluxes. As the original spaxels (0.05 arcsec × 0.05 arcsec) are smaller than the angular resolution of our observations, this procedure does not affect the spatial resolution of the maps significantly. The line emission is more extended along PA = 60/240°, extending up to 1.5 arcsec on both sides of the nucleus, while in the perpendicular direction (PA = −30/150°), the emission is extended to 0.7 arcsec from the nucleus. The flux distributions of all emission lines show good correlation with the radio structures, with the two peaks of emission associated with the south-western and north-eastern radio hotspots. Some differences are observed among distinct flux distributions. While the [Fe II] and

Table 1. Measured emission-line fluxes for the five positions along PA = 60° and PA = −30° within 0.35 arcsec × 0.35 arcsec aperture in units of 10^{-16} erg s^{-1} cm^{-2}.

λ_{vac} (Å)	ID	0.50 arcsec NE	0.60 arcsec SW	Nucleus	0.35 arcsec SE	0.35 arcsec NW
11 471.3	[P II] $^1D_3 - {}^3P_1$	12.1±5.3	6.3 ± 4.3	–	–	–
11 665.6	[Fe II] $b^4P_{1/2} - a^2P_{3/2}$	21.1 ± 4.8	–	–	–	–
11 863.7	[Fe II] $b^4D_{1/2} - b^4F_{5/2}$	10.4 ± 5.7	–	–	–	–
11 886.1	[P II] $^1D_2 - {}^3P_2$	18.3 ± 4.4	26.9 ± 8.6	–	–	–
12 570.2	[Fe II] $a^4D_{7/2} - a^6D_{9/2}$	179.4 ± 15.3*	299.9 ± 18.0**	110.2 ± 8.2*	35.0 ± 8.5*	110.1 ± 9.3*
12 791.2	[Fe II] $a^4D_{3/2} - a^6D_{3/2}$	9.9 ± 2.3	4.7 ± 1.2	–	–	14.6 ± 9.5*
12 821.6	H I Pa β	117.3 ± 5.2	106.1 ± 10.8	79.0 ± 9.3*	29.1 ± 4.4*	157.9 ± 12.1*
12 946.2	[Fe II] $a^4D_{5/2} - a^6D_{5/2}$	13.4 ± 4.4	5.5 ± 3.3	18.6 ± 9.5*	0.70 ± 0.13*	17.8 ± 14.1*
13 209.2	[Fe II] $a^4D_{7/2} - a^6D_{7/2}$	60.9 ± 20.4*	69.0 ± 7.8	13.6 ± 8.2*	2.21 ± 0.26*	24.5 ± 20.9*
13 281.4	[Fe II] $a^4D_{5/2} - a^6D_{3/2}$	18.8 ± 11.2	–	–	–	–
21 218.3	H_2 2 1-0S(1)	18.7 ± 1.7	45.7 ± 1.5	27.1 ± 7.4*	16.8 ± 4.8*	16.5 ± 3.0*
21 542.0	H_2 1-0 S(2)	1.9 ± 0.7	2.1 ± 0.6	–	3.8 ± 2.9*	–
21 661.2	H I Br γ	16.4 ± 1.5	14.5 ± 1.3	12.9 ± 2.4*	10.5 ± 3.0*	12.5 ± 3.5*
22 234.4	H_2 1-0 S(0)	9.4 ± 0.7	11.4 ± 0.6	–	–	–
22 477.6	H_2 2-1 S(1)	4.9 ± 0.62	5.2 ± 1.0	–	–	–
24 084.7	H_2 1-0 Q(1)	21.8 ± 1.3	39.5 ± 0.7	25.8 ± 6.8*	13.8 ± 6.4*	15.5 ± 6.0*
24 136.7	H_2 1-0 Q(2)	6.3 ± 2.5	7.9 ± 1.9	–	–	–
24 218.0	H_2 1-0 Q(3)	18.0 ± 2.8	32.3 ± 2.8	25.0 ± 14.4*	15.4 ± 9.9*	17.6 ± 13.1*
24 369.7	H_2 1-0 Q(4)	–	12.6 ± 1.9	–	–	–
24 548.5	H_2 1-0 Q(5)	14.3 ± 3.6	22.9 ± 4.7	–	–	–
24 755.5	H_2 1-0 Q(6)	–	8.4 ± 4.1	–	–	–
25 000.7	H_2 1-0 Q(7)	–	10.5 ± 8.2	–	–	–

Notes. *Emission-line profile fitted by two Gaussian curves and the flux represents the sum of the fluxes of both components; **Emission-line profile fitted by three Gaussian curves and the flux represents the sum of the fluxes of the components.

H_2 fluxes peak at the location of the south-western radio structure at 0.6 arcsec from the nucleus, the highest fluxes of the H I recombination lines are at the location of the north-eastern radio hotspot at 0.50 arcsec from the nucleus. Another difference is that the H_2 emission is less collimated and more extended in all directions, as most clearly seen in the H_2 λ2.1218 flux distribution [which has the highest signal-to-noise (S/N) ratio among the H_2 lines].

3.3 Line-ratio maps

The excitation mechanisms of the [Fe II] and H_2 emission lines can be investigated using emission-line-ratio maps. Fig. 4 shows the [Fe II] λ1.2570 μm/[P II] λ1.8861 μm (top-left panel), [Fe II] λ1.2570 μm/Pa β (top-right panel), H_2 λ2.1218 μm/Br γ (bottom-left panel) and H_2 λ2.2447 μm/H_2 λ2.1218 μm (bottom-right panel) line-ratio maps. The first two are useful for investigating the origin of the [Fe II] emission and the last ones for investigating the origin of the H_2 emission.

The [Fe II]/[P II] map has values ranging from ∼2 to 10, with the highest values observed at the location of the north-eastern radio knot and the lowest values at regions next to the nucleus of the galaxy. At the position of the south-western radio knot, [Fe II]/[P II] is ∼7. The [Fe II]/Pa β line ratio has values ranging from 0.5 up to 3.5, with the highest values observed in regions next to the south-western radio knot. A small enhancement in this ratio is also observed next to the north-eastern radio knot, where the values are approximately 2.5. At most locations, the [Fe II]/Pa β ratio has values in the range 0.6–2.0. Values smaller than 0.6 are observed only in a small region at 0.5 arcsec north-north-east of the nucleus.

The H_2/Br γ line ratio has values in the range 0.2–4.5, with the highest values observed in regions surrounding the south-western radio knot and at the nucleus. For most locations, the values of H_2/Br γ are in the range 0.6–2.0 and the smallest values of 0.3 are observed at 0.5 arcsec north-north-east of the nucleus, at the same location where the [Fe II]/Pa β ratio map has its smallest value. Finally, the H_2 λ2.24/2.12 ratio map has values ranging from 0.1 to 0.3 with the highest values seen at 0.5 arcsec north-east of the nucleus, associated with the radio knot there.

In Fig. 5, we present a reddening map obtained from the Pa β/Br γ line ratio using

$$E(B-V) = 4.74 \log \left(\frac{5.88}{F_{\mathrm{Pa}\,\beta}/F_{\mathrm{Br}\,\gamma}} \right), \quad (1)$$

where $F_{\mathrm{Pa}\,\beta}$ and $F_{\mathrm{Br}\,\gamma}$ are the fluxes of the Pa β and Br γ emission lines, respectively. We have adopted the intrinsic ratio $F_{\mathrm{Pa}\,\beta}/F_{\mathrm{Br}\,\gamma} = 5.88$ corresponding to case B recombination (Osterbrock & Ferland 2006) and used the reddening law of Cardelli, Clayton & Mathis (1989). The values of $E(B-V)$ for NGC 5929 range from 0 to 2, with the highest values observed to the south, south-east and east of the nucleus, while smaller values are observed approximately along the region covered by the radio jet at PA ≈ 45°, from the north-east to the south-west of the nucleus.

3.4 Stellar kinematics

The *K*-band spectra of Fig. 1 show clearly the CO absorption bandheads around 2.3 μm. We used the penalised pixel-fitting (PPXF) method of Cappellari & Emsellem (2004) to fit these bands and obtain the line-of-sight velocity distributions of the stars, using the Gemini library of late spectral type stars observed with the Gemini Near-Infrared Spectrograph (GNIRS) Integral Field Unit (IFU) and NIFS (Winge, Riffel & Storchi-Bergamann 2009) as templates. The stellar line-of-sight velocity distribution was approximated by a Gaussian distribution. PPXF outputs the stellar radial velocity (V_*), the corresponding velocity dispersion (σ_*), as well as the uncertainties for both parameters at each spaxel.

Fig. 6 presents the resulting maps for V_* and σ_*. The S/N ratio of the spectra at locations next to the borders of the field of view

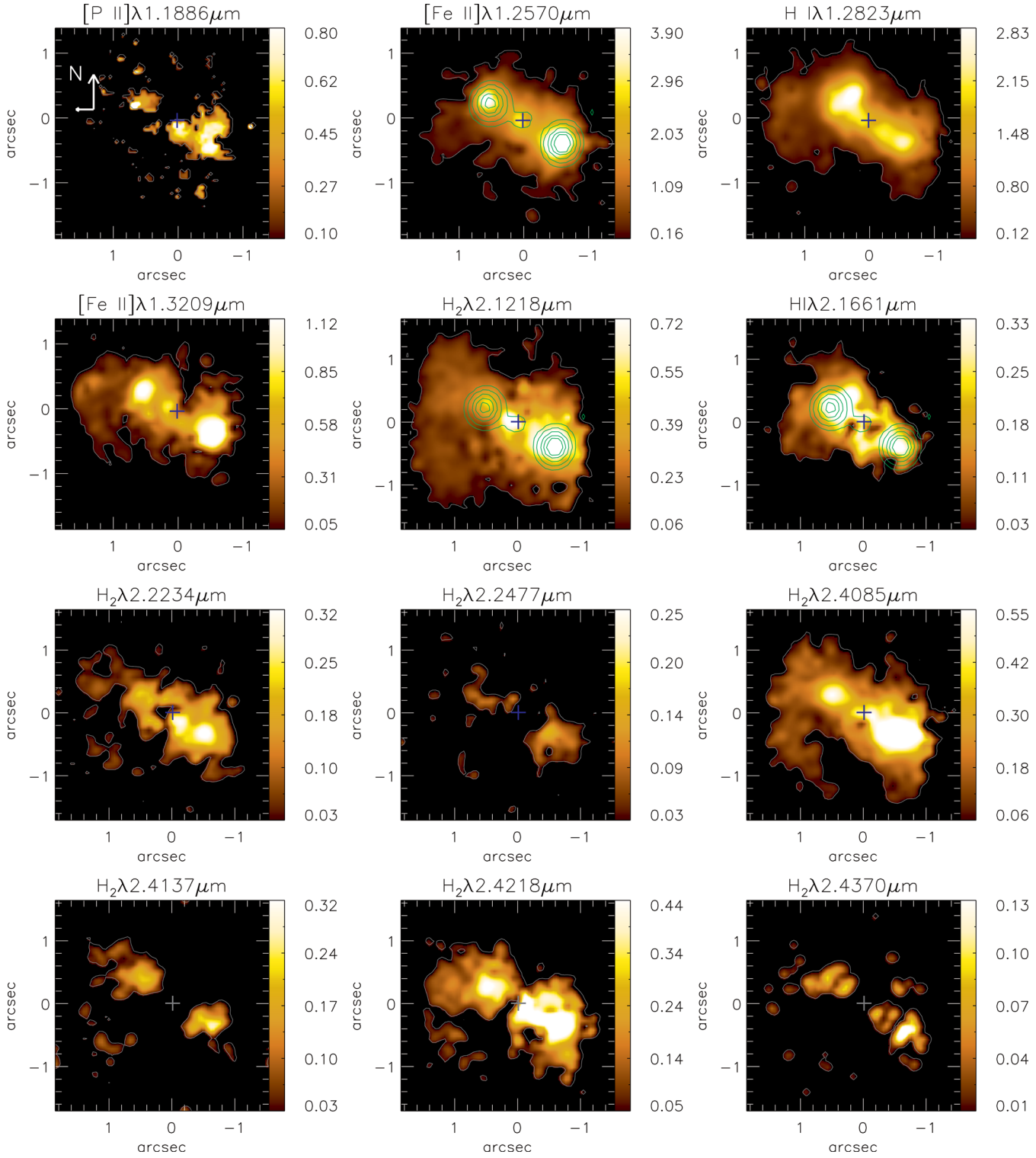

Figure 3. Integrated flux maps for the emission lines identified at the top of each panel, in units of 10^{-17} erg s^{-1} cm^{-2}. The central cross marks the position of the continuum peak. The green contours overlaid on some maps are from the 6 cm radio continuum image from Ulvestad & Wilson (1989).

was too low and we could not obtain good fits. These borders were then masked out. The white (black) regions in the V_* (σ_*) map correspond to these locations, where the uncertainties in V_* or σ_* are larger than 30 km s^{-1}. The stellar velocity field shows a velocity amplitude of about 100 km s^{-1}, with red shifts to the north-east and blue shifts to the south-west, thus opposite from the rotation field observed for the gas, which has red shifts to the south-west and blue shifts to the north-east, as observed in Fig. 7. The σ_* map shows values ranging from 40 to 180 km s^{-1} with a median value of $\sigma_* = 114 \pm 7$ km s^{-1} and there is a partial ring of lower σ_* values (60–100 km s^{-1}) with a radius of 0.5 arcsec surrounding the nucleus.

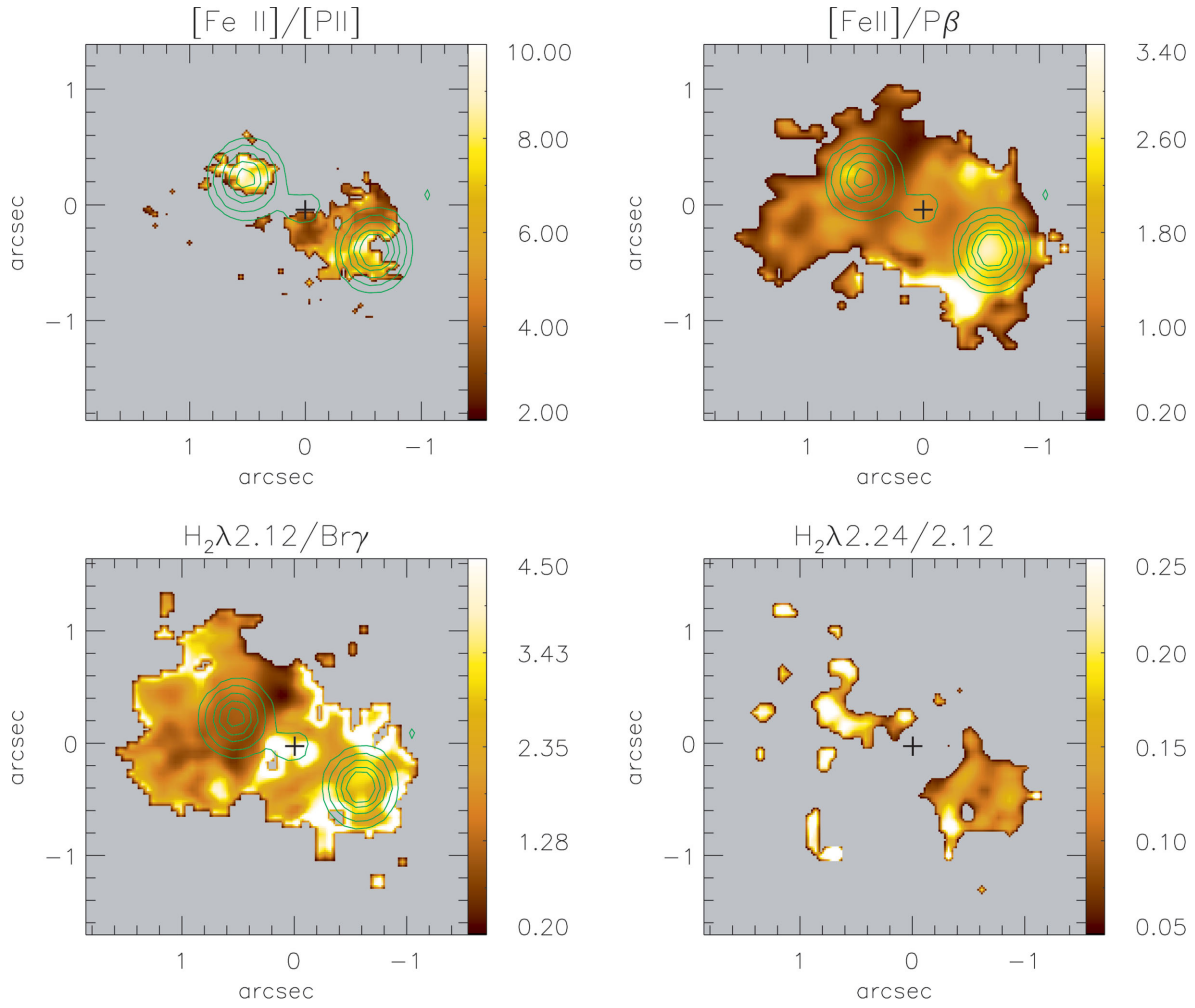

Figure 4. Top: [Fe II] λ1.25 μm/[P II] λ1.8861 μm (left) and [Fe II] λ1.2570 μm/Pa β line-ratio map (right). Bottom: H_2 λ2.1218 μm/Br γ (left) and H_2 λ2.2447 μm/H_2 λ2.1218 μm (right). The green contours overlaid to the [Fe II]/[P II], [Fe II]/Pa β and H_2/Br γ maps are from the 6 cm radio image, the cross marks the position of the continuum peak. The grey areas are masked regions following the same criteria used in the flux maps. The green contours overlaid to some panels are from the 6 cm radio image of Ulvestad & Wilson (1989) and the cross marks the position of the peak of the continuum emission.

3.5 Gas kinematics

We used the centroid wavelength of the emission lines [P II] λ1.1886 μm, [Fe II] λ1.2570 μm, Pa β and H_2 λ2.1218 μm at each position to map the velocities of the ionized-gas forbidden lines, ionized-gas permitted lines and molecular gas. These lines have been chosen because they have the highest S/N ratios among their species.

These maps are shown in Fig. 7. The white regions are masked due to bad fits, following the same criteria used for the flux distributions of Fig. 3. All velocity maps show red shifts of up to 220 km s^{-1} to the south-west of the nucleus and blue shifts of similar amplitude to the north-east of it. The zero velocity line is oriented approximately along PA = −30/150°, coincident with the strip where the lines are doubled.

Fig. 8 presents the corresponding velocity dispersion (σ) maps. The σ values for all emission lines are in the range 30–200 km s^{-1}. At most locations, σ is lower than 100 km s^{-1}. The highest σ values are observed along the SE-NW strip (which has a width of ∼0.3 arcsec, thus 50 pc at the galaxy), crossing the nucleus perpendicular to the radio jet, and they are due to the double components observed in the emission lines at these locations. These

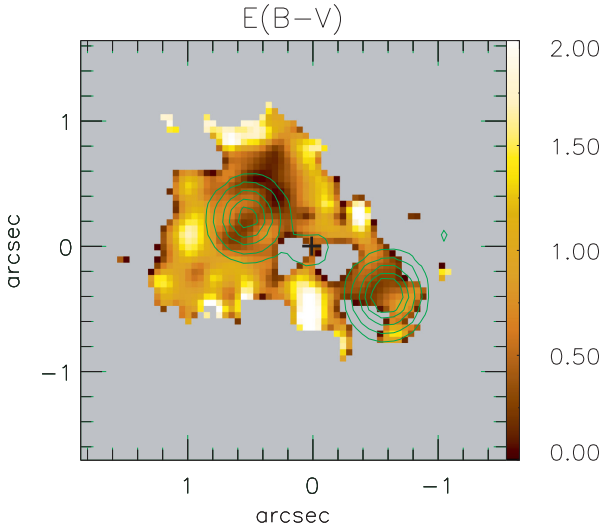

Figure 5. Reddening map obtained from the Pa β/Br γ line ratio. Green contours are from the radio image and the central cross marks the position of the nucleus.

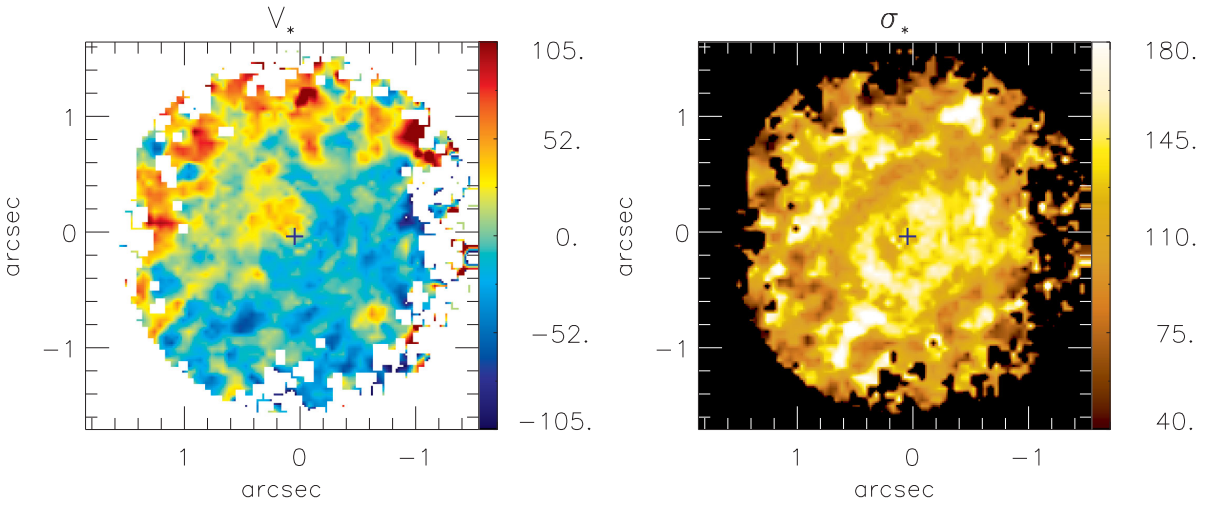

Figure 6. Stellar velocity (V_*) field (left) and corresponding velocity dispersion (σ_*) map (right). The central cross marks the position of the nucleus, the colour bars show V_* and σ_* values in units of km s^{-1} and the white (black) regions in the V_* (σ_*) map represent the locations where we could not get good fits of the galaxy spectra.

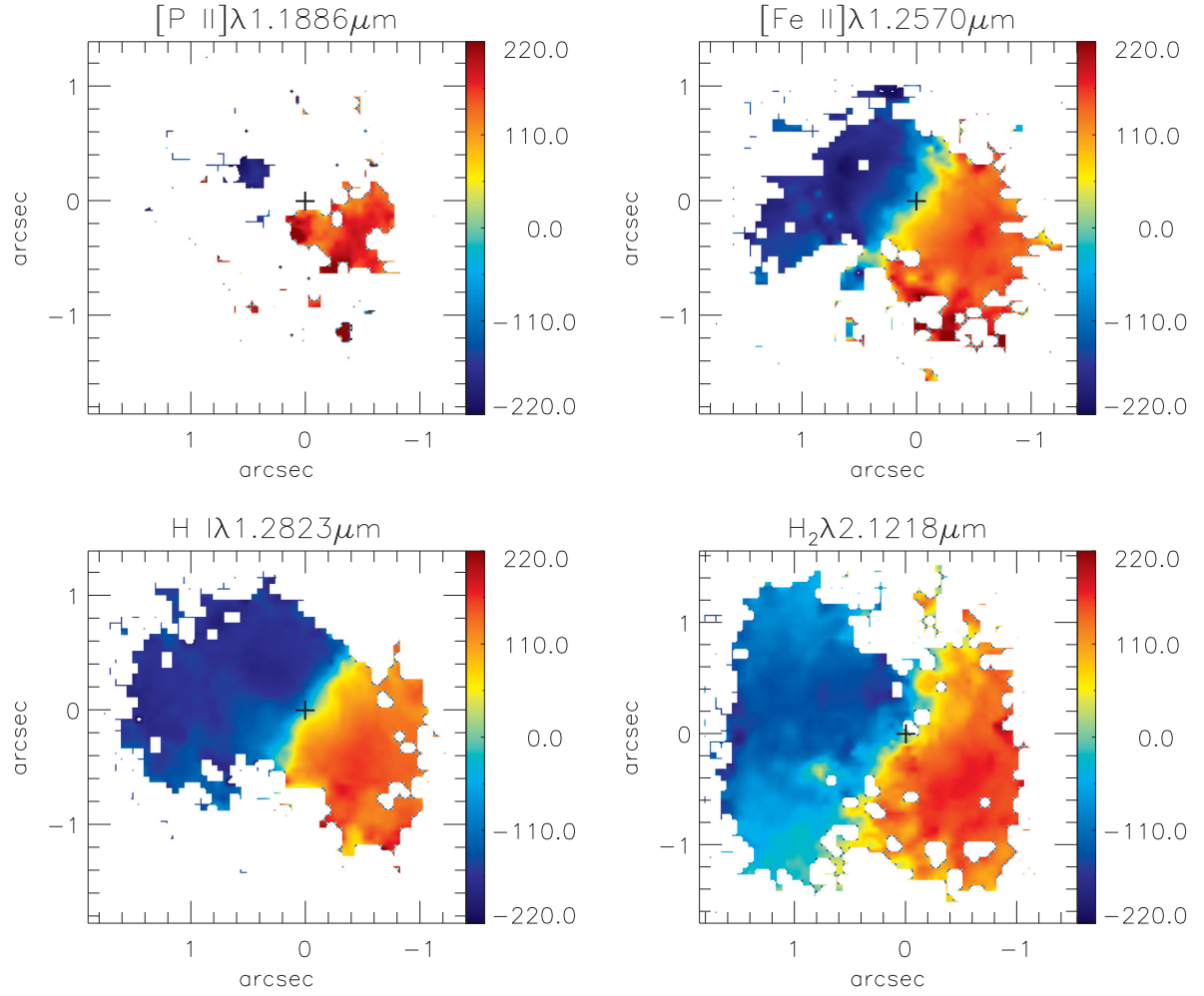

Figure 7. Centroid velocity maps derived from the fit of the [P II] λ1.1886 μm, [Fe II] λ1.2570 μm, Pa β and H_2 λ2.1218 μm emission-line profiles using a single Gaussian. The central cross marks the position of the nucleus and the scale for the colour bar is in units of km s^{-1}.

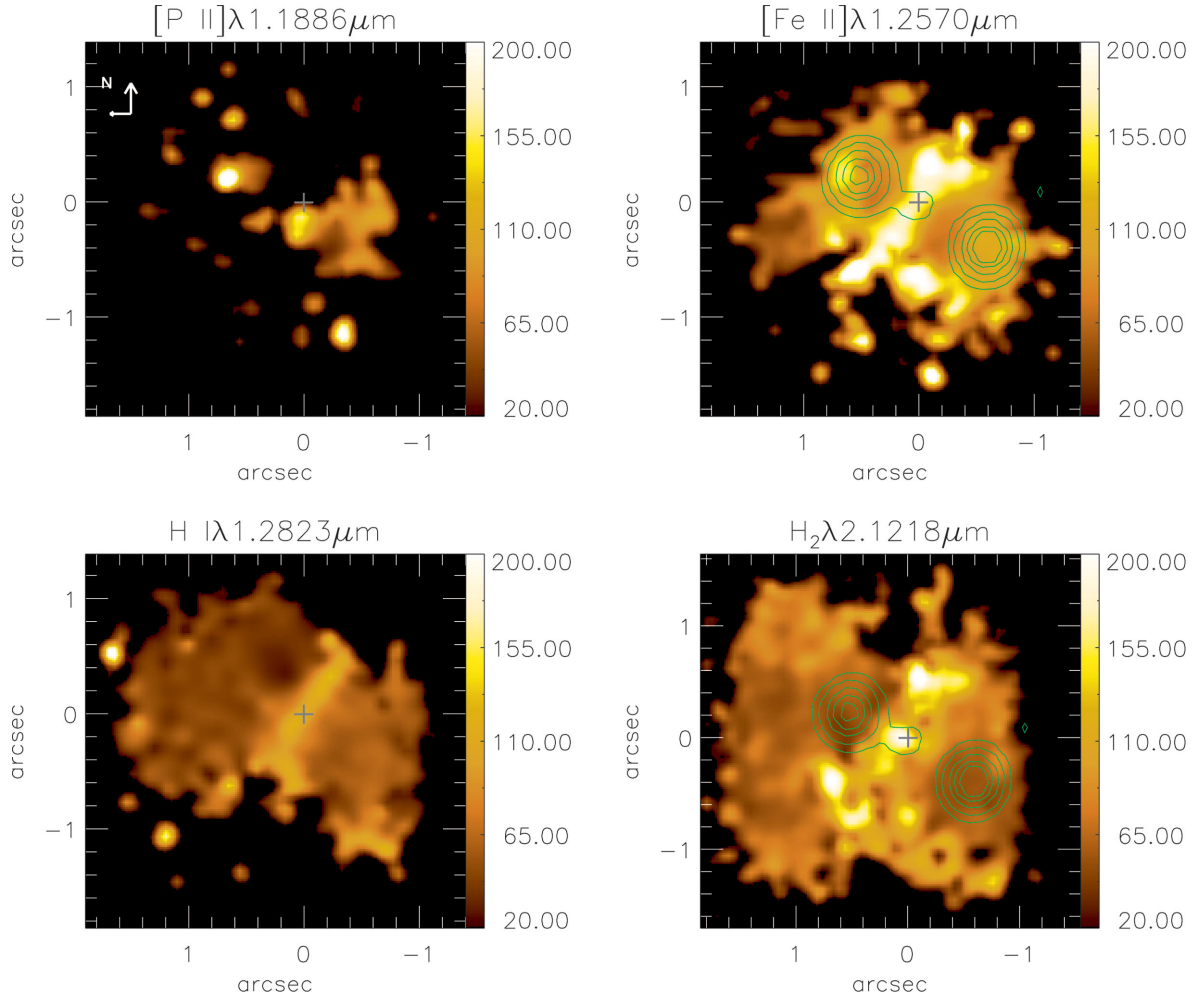

Figure 8. Velocity dispersion maps derived from the [P II] λ1.1886 μm, [Fe II] λ1.2570 μm, Pa β and H_2 λ2.1218 μm emission-line profiles. The central cross marks the position of the nucleus, the scale for the colour bar is in units of km s^{-1} and the green contours are from the 6 cm radio image of Ulvestad & Wilson (1989).

double components were attributed to an equatorial outflow in Paper I, where we presented the results only for [Fe II]. Now we compare the [Fe II] and [P II] maps with those of Pa β and H_2 and we find some differences. The [Fe II] and [P II] maps show that, besides the high σ values observed along the SE-NW strip, there is also an increase of σ at and around the locations of the radio hotspots. The Pa β and H_2 maps, on the other hand, do not show any evidence of increased σ there. A comparison between the profiles of these lines at the location of the radio hotspots can be seen in Fig. 2; it is clear that the profile of the [Fe II] line is broader than those of the Pa β and H_2 lines as reported in Paper I, being attributed to the interaction of the radio jet with the ambient gas.

3.6 Channel maps

In Figs 9, 10 and 11 we show velocity-channel maps along the Pa β, [Fe II] and H_2 emission-line profiles, respectively. The H_2 channel maps show emission for a velocity range from approximately −300 to 300 km s^{-1}, with the emission moving from north-east to south-west as the velocity increases, being consistent with a rotating disc. At low velocities, the Pa β channel maps are similar to that observed for H_2, but additional Pa β emission from high-velocity gas is observed associated with the radio hotspots to the north-east at the blue-shifted channels and to the south-west at the red-shifted channels. This suggests an interaction of the radio hotspots with the Pa β emitting gas. For the [Fe II] emission, the correlation of the line emission with the radio hotspots is clearer with emission being observed at velocities down to −560 km s^{-1} at blue shifts and up to 500 km s^{-1} at red shifts.

4 DISCUSSION

4.1 Emission-line flux distributions

All emission lines have flux distributions more extended along PA = 60/240°, which is the orientation of the radio jet (Ulvestad & Wilson 1989; Su et al. 1996). The companion galaxy NGC 5930 is also at PA = 60°. Along the perpendicular direction, the line emission extends only to ∼0.7 arcsec from the nucleus for most lines (a bit more for H_2). In particular, along the SE-NW strip, we concluded in Paper I that the gas is outflowing from the nucleus.

Although the bulk of the emission-line flux distributions is similar for all species, some differences are observed: (i) while the flux in the H I recombination lines peaks at 0.5 arcsec north-east of the nucleus, the [Fe II], [P II] and H_2 lines peak at 0.6 arcsec south-west of the nucleus; and (ii) the [Fe II], [P II] and H I lines are more

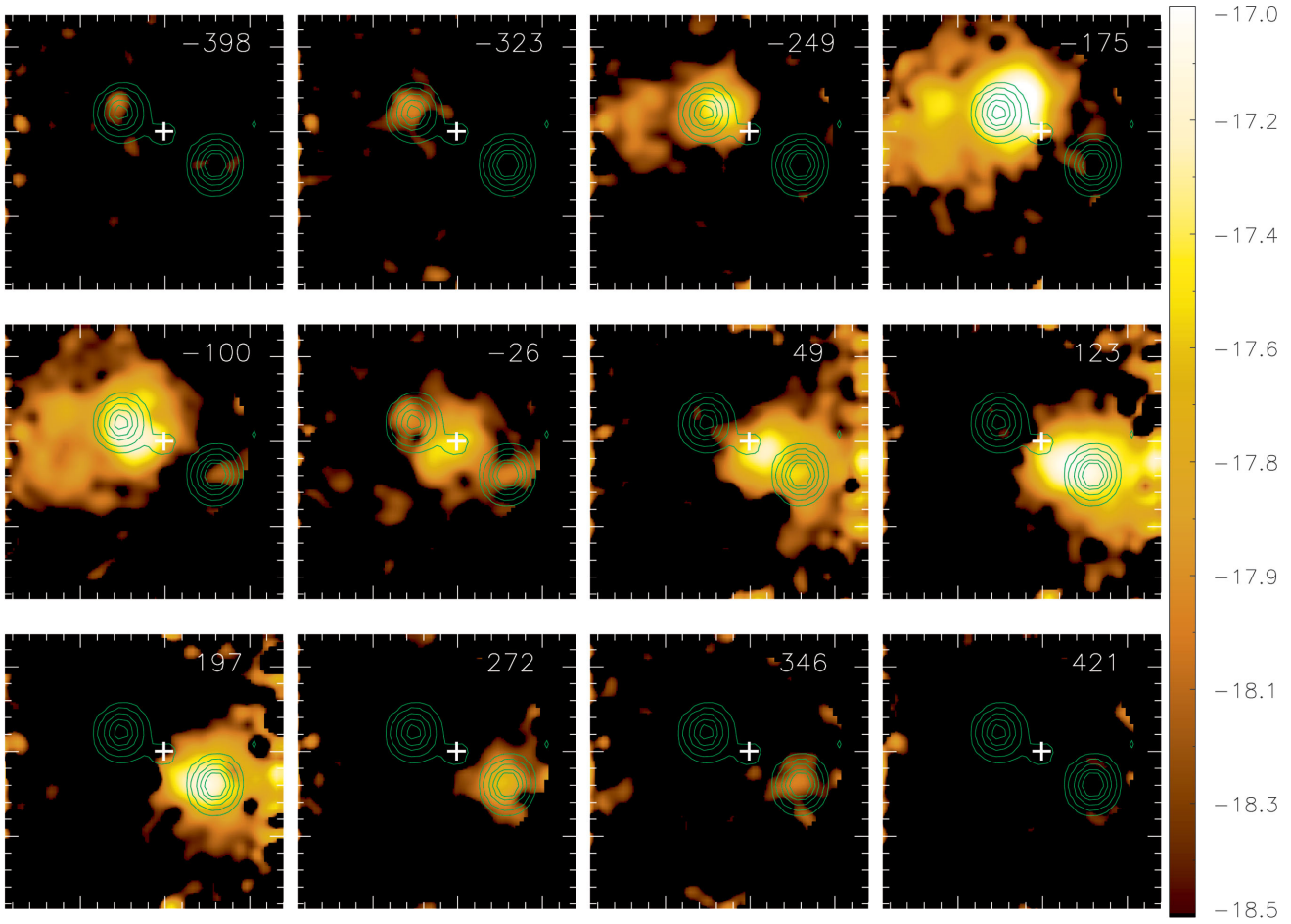

Figure 9. Channel maps along the Pa β line profile for a velocity bin of 75 km s^{-1}, corresponding to three spectral pixels. The corresponding velocity is shown in the top-right corner of each panel in units of km s^{-1} and the green contours are from the radio jet. The colour bar shows the flux scale in logarithmic units.

collimated along the radio axis than the H_2 emission. There are similar differences between the flux distributions (and kinematics) of the ionized gas and molecular gas for most of the Seyfert galaxies we have studied so far in this project (Riffel et al. 2006, 2008, 2009, 2010a, 2014a; Riffel & Storchi-Bergmann 2011a; Storchi-Bergmann et al. 2009, 2010; Riffel & Storchi-Bergmann 2011b; Schönel et al. 2014).

We also note that the flux values along the SE-NW strip are lower than along the direction of the radio jet, revealing that the outflowing gas discovered in Paper I does not contribute much to the total luminosity. This is consistent with the interpretation that the radiation from the AGN escapes mainly along the ionization axis, which seems to be coincident with the radio axis and is blocked along the perpendicular direction due to the dusty torus postulated by the AGN unified model. This interpretation is supported by our discussion in Section 4.7, in which we conclude that X-ray heating (as X-rays can escape through the torus) is the main excitation mechanism of the H_2 emission of both kinematic components observed along PA $= -30/150^{\circ}$.

We compare our results with previous ones from the literature. Optical IFS was obtained for NGC 5929 by Ferruit et al. (1997) at a seeing of 0.8 arcsec and by Stoklasová et al. (2009) with the instrument OASIS at the Canada France Hawaii Telescope (CFHT) in the low spatial resolution mode (0.4 arcsec sampling). Ferruit et al. (1997) present a contour map for the [N II]+Hα emission, showing that it is more extended along the PA of the radio jet and with the peak of emission observed at ∼0.6 arcsec south-west of the nucleus, in good agreement with our flux distributions in the near-IR. Stoklasová et al. (2009) present flux and kinematic maps for [O III] λ5007, H β and [N I] $\lambda\lambda$5198, 5200, finding similar flux distributions to that of Ferruit et al. (1997). Although the optical emission-line flux distributions are also more extended along PA $= 60/240^{\circ}$, as we observe, the optical lines do not show an emission peak to the north-east, as we have observed for the near-IR lines. We attribute these differences to the worse spatial resolution of the optical observations. This interpretation is supported by the work of Rosario et al. (2010), who present a *HST* narrow-band image for the [O III]+$H\beta$ emission that clearly shows two main emission regions, one to the north-east and the other to the south-west, with the highest fluxes observed to the south-west, in good agreement with the [Fe II], [P II] and H_2 flux distributions.

Why do the near-IR H I recombination lines have flux distributions distinct from that of H β in the flux map of Stoklasová et al. (2009)? As seen in Fig. 3, the Pa β and Br γ flux maps have peaks at 0.5 arcsec north-east of the nucleus with secondary peaks at 0.6 arcsec south-west of it. On the other hand, the H β flux distribution has an emission peak to the south-west and although the emission is also extended to the north-east, there is no emission

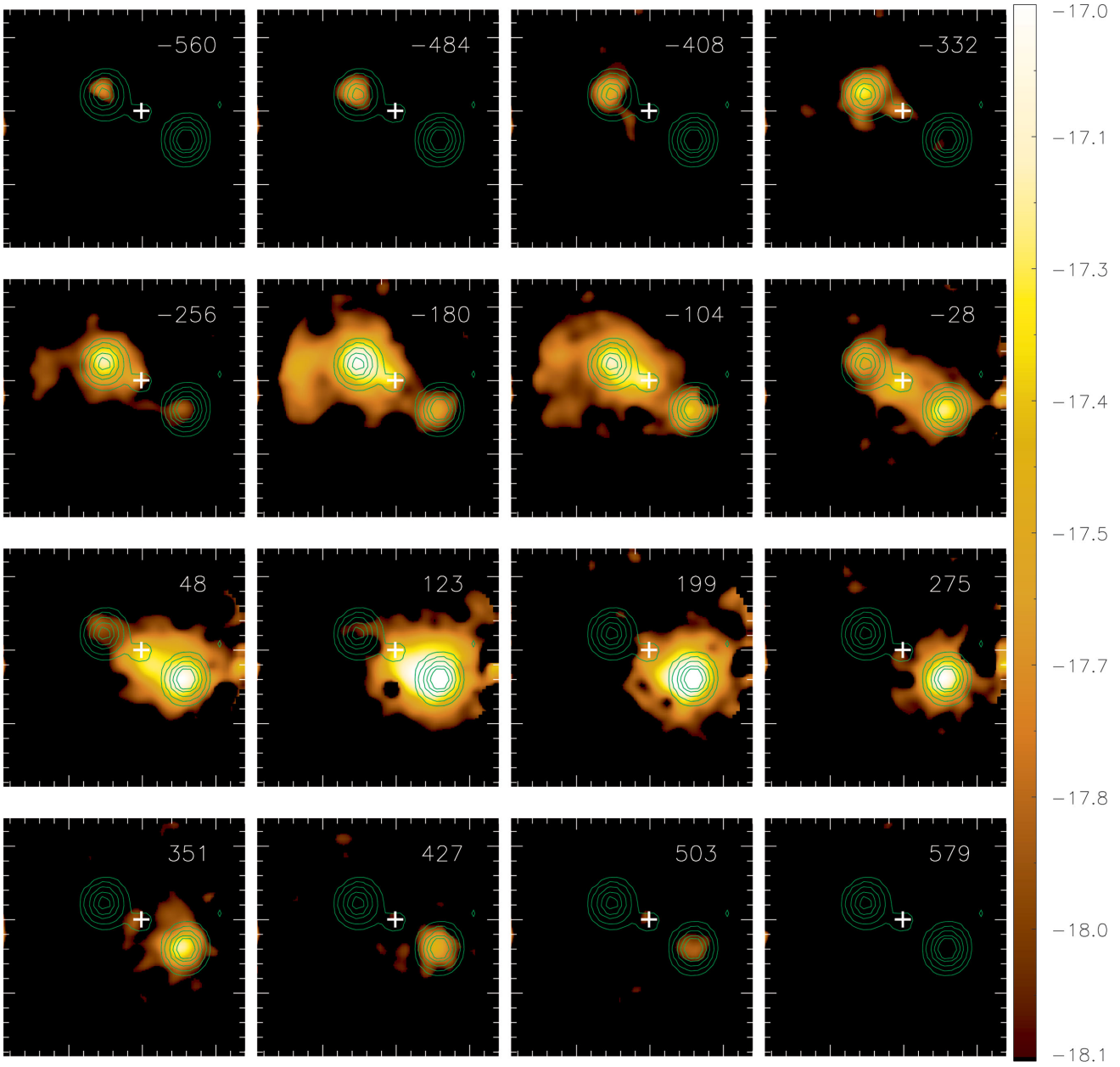

Figure 10. Same as Fig. 9 for the [Fe II] λ1.2570 μm emission line.

peak as observed for the near-IR lines. We attribute this difference to dust extinction, which is stronger in the optical than in the near-IR. Indeed, as seen in Fig. 5, the reddening is somewhat larger to the east and north-east of the nucleus supporting the conclusion that the near-IR emission is probing a dustier region than the optical emission. A difference of 0.5 mag in $E(B-V)$ between the north-east and south-west sides corresponds to a ratio of 2.2 between the Pa β fluxes of the north-east and south-west using the Cardelli et al. (1989) extinction law, while for H β the ratio would be higher, ∼2.9. This difference would be enough to make the north-eastern hotspot brighter than the south-western hotspot in the H β flux map of Stoklasová et al. (2009), supporting our conclusion that the difference between the near-IR and optical flux distributions is due to extinction.

4.2 Stellar kinematics and the mass of a supermassive black hole

The stellar velocity field (left-hand panel of Fig. 6) shows a rotation component, with the north-eastern side of the disc approaching and the south-western side receding with a velocity amplitude of about 80 km s^{-1}. To derive the systemic velocity (V_s), orientation of the line of nodes (Ψ_0), inclination (i) and eccentricity (e) of the disc, we fitted the stellar velocity field using the DISKFIT code (Spekkens & Sellwood 2007; Sellwood & Sánchez 2010; Kuzio et al. 2012).

The best rotating disc model is shown in the top-centre panel of Fig. 12. The observed velocity field is shown in the top-left panel and the residual map in the top-right panel of the same figure, respectively. The corresponding kinematic parameters are shown in Table 2.

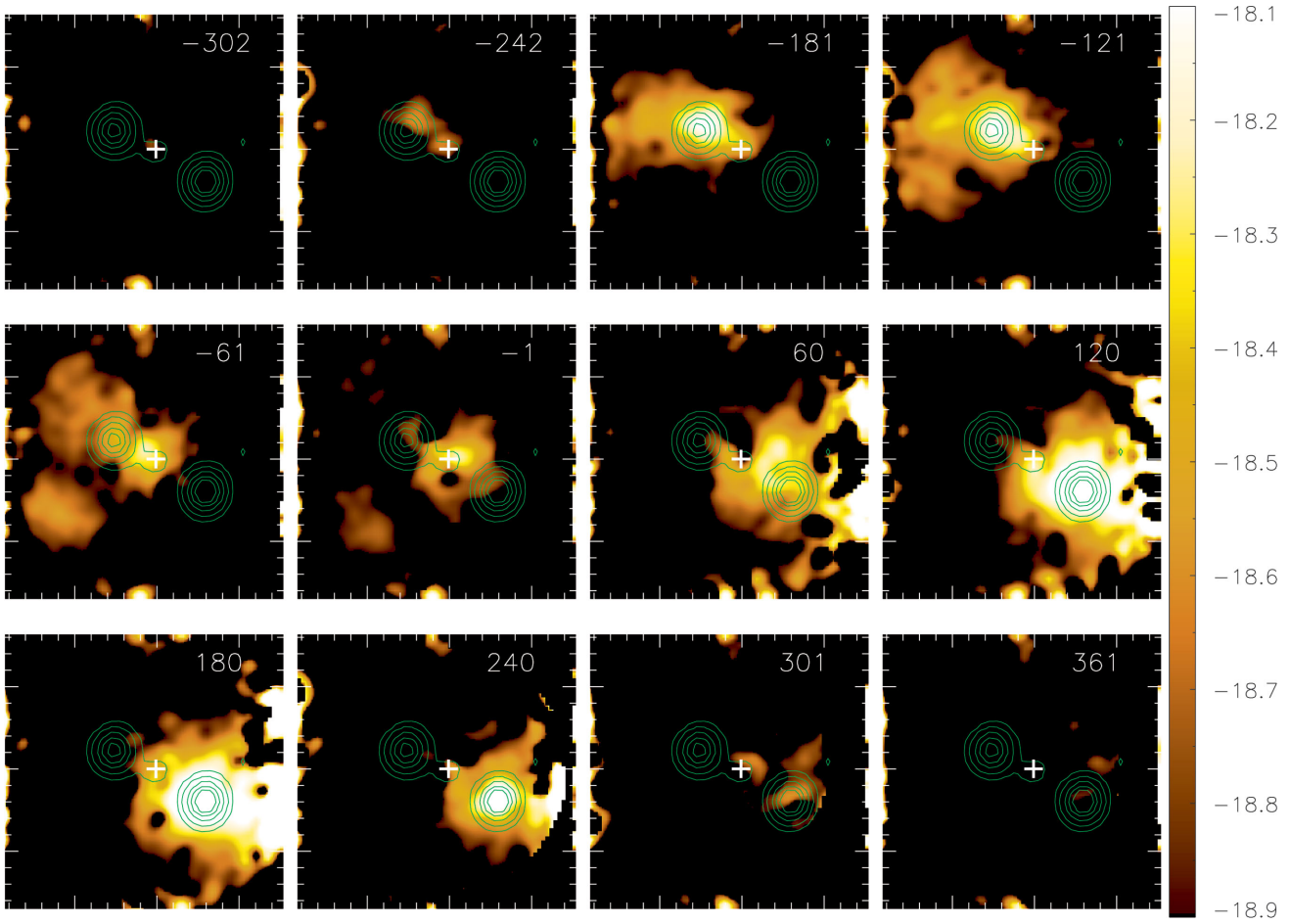

Figure 11. Same as Fig. 9 for the H_2 λ2.1218 μm emission line for a velocity bin of 60 km s^{-1}, corresponding to two spectral pixels.

The stellar velocity dispersion (σ_*) can be used to estimate the mass of the supermassive black hole ($M_\bullet$) at the centre of NGC 5929, using the $M_\bullet$–σ relation. We obtain $\sigma_* = 133 \pm 8$ km s^{-1} using PPXF for an integrated K spectrum over the whole field of view. $M_\bullet$ can be estimated by (Kormendy & Ho 2013):

$$\log\left(\frac{M_\bullet}{10^9\,M_\odot}\right) = -(0.500 \pm 0.049) + (4.420 \pm 0.295) \times \log\left(\frac{\sigma}{200\,\mathrm{km\,s^{-1}}}\right).$$

We estimated a mass of $M_\bullet = 5.2^{1.6}_{-1.2} \times 10^7$ M$_\odot$. Using the relation from Graham & Scott (2013) for non-barred galaxies, we obtain a smaller mass of $M_\bullet = 1.74^{0.65}_{-0.45} \times 10^7$ M$_\odot$.

The central velocity dispersion quoted in the Hyperleda data base (Paturel et al. 2003) is $\sigma_* = 120.6 \pm 12.9$ km s^{-1}, and results in $M_\bullet = 3.4^{3.3}_{-1.9} \times 10^7$ M$_\odot$.

4.3 Gas kinematics

4.3.1 Equatorial outflow

In Paper I, we reported the discovery of a peculiar gas outflow along the SE-NW strip, which has a width of ∼50 pc and an extent of ∼300 pc along PA = −30/150°, perpendicular to the radio jet. At locations away from the SE-NW strip, the gas kinematics is consistent with orbital motion in a disc that is counter-rotating relative to the stellar disc. This rotation component is clear in our Fig. 7, which is based on a single-Gaussian fit to the emission-line profiles and can be compared to the stellar velocity field shown in the left-hand panel of Fig. 6. Our stellar and gas velocity fields are very similar to those presented by Stoklasová et al. (2009), which were derived from optical IFS, although they did not detect the outflow in the SW-NW strip due to the poorer spatial resolution.

To show the distinct kinematic components better along the SE-NW strip, where the mass outflow was observed in Paper I, we extracted one-dimensional cuts from the [Fe II] flux distribution, velocity field and σ map for the two components along the strip. The σ of the two components was kept the same, as done in Paper I. These cuts are shown in Fig. 13, where it can be seen that the velocities of the two components are almost constant along the strip, −150 and 150 km s^{-1} relative to the systemic velocity of the galaxy for the blue and red components, respectively. The fluxes of both components are similar at most locations, with the red component being brighter at distances smaller than 0.5 arcsec from the nucleus to the south-east. These components were attributed to the presence of an equatorial outflow (perpendicular to the radio jet) in Paper I. Such gas outflows appear in recent theoretical models of accretion disc winds (Li, Ostriker & Sunyaev 2013) as well as in outflowing torus models (e.g., Hönig et al. 2013; Elitzur 2012), in which the outflows originated as a consequence of the conservation of the gas angular momentum.

We can use the observed velocity and geometry of the emitting gas to estimate its mass outflow rate ($\dot{M}$) in the equatorial outflow. The double components observed along PA = −30/150° are attributed to

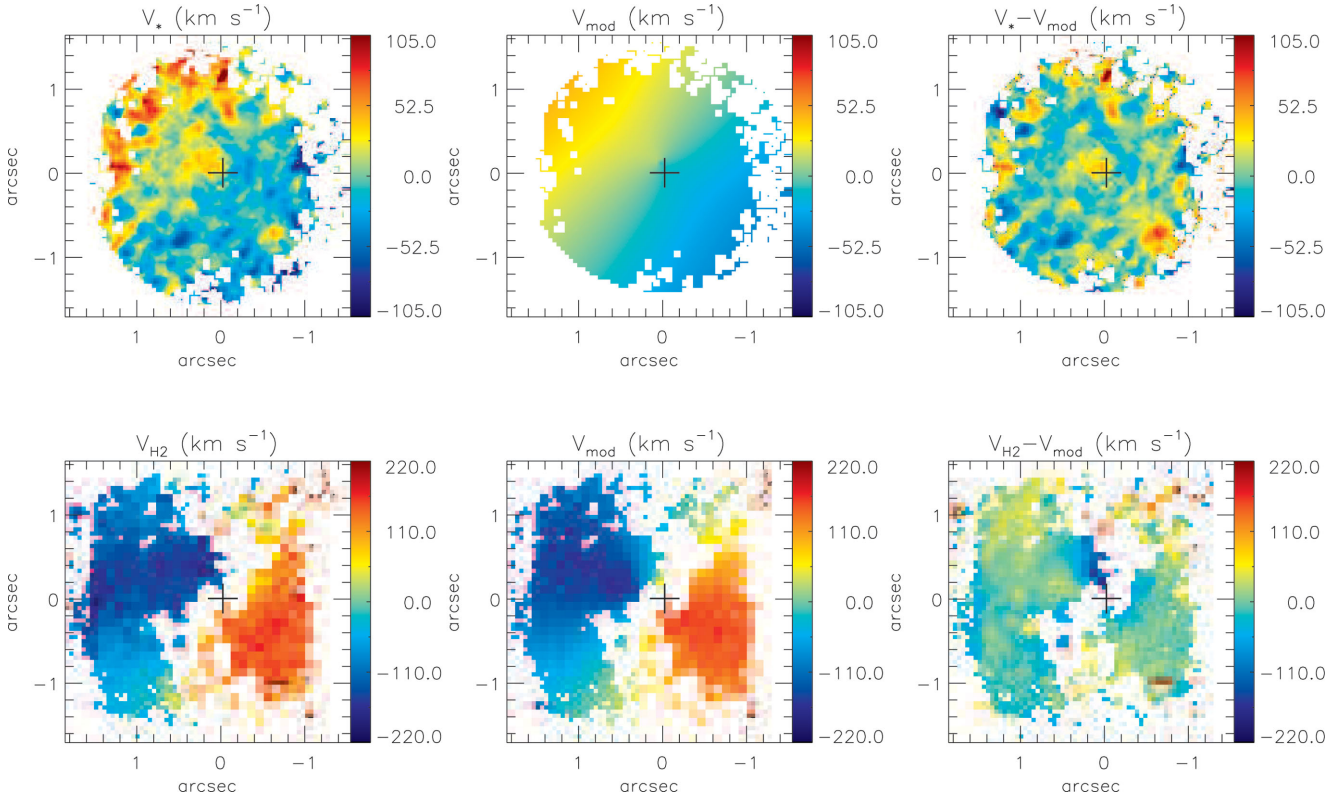

Figure 12. From left to right: Observed velocity field, rotating disc model and residual map (observed versus model) for the stellar (top) and H_2 (bottom) velocity fields. The colour bars show the range of velocities in units of km s^{-1} relative to the systemic velocity of the galaxy and the central cross marks the position of the nucleus.

Table 2. Kinematic parameters for the best rotating disc model. Col 1: Fitted velocity field, col 2: heliocentric systemic velocity, col 3: orientation of the line of nodes, col 4: ellipticity, col 5: inclination of the disc and col 6: position of the kinematical centre relative to the peak of the *K*-band continuum emission.

Velocity field	V_s (km s^{-1})	Ψ_0	e	i	(X_{cen}, Y_{cen})
H_2	2500.1 ± 17.4	25.7° ±1.3°	0.05 ± 0.02	18.4° ±1.2°	(0.2 ± 0.1 arcsec, −0.1 ± 0.1 arcsec)
Pa β	2472.8 ± 18.5	36.5° ±1.1°	0.05 ± 0.02	18.2° ±1.3°	(−0.1 ± 0.1 arcsec, 0.0 ± 0.1 arcsec)
[Fe II]	2469.3 ± 18.5	25.4° ±4.4°	0.05 ± 0.04	18.2° ±7.8°	(0.1 ± 0.1 arcsec, 0.0 ± 0.1 arcsec)
Stars	2489.4 ± 17.1	219.9° ±1.3°	0.05 ± 0.03	18.2° ±6.7°	(0, 0) fixed

the equatorial outflow from the nucleus. As the outflow is observed as two similar velocity components, one in red shift and the other in blue shift, we considered a scenario in which the outflow has generated a hollow cylinder of outflowing mass. Considering the width of the SE-NW strip (50 pc) as being the height (h) of a cylinder with radius R_0, the mass outflow rate can be estimated by

$$\dot{M} = m_p N_e v f A, \quad (2)$$

where m_p is the proton mass, N_e the electron density, v is the velocity of the outflowing gas, f is the filling factor and $A = 2\pi R_0 h$ is the lateral area of the cylinder. As the velocity of the outflow is approximately constant along the strip and the velocity does not decrease as a function of distance from the centre to the north-west and south-west, we conclude that this cylinder has a large radius, at least the size of the region where emission is observed, $R_0 > 0.5$ arcsec.

Assuming $N_e = 500\,\mathrm{cm}^{-3}$, $f = 0.01$ (which are typical values estimated for other Seyfert galaxies, e.g., Schnorr-Müller al. 2011, 2014a,b; Storchi-Bergmann et al. 2010), $v = 110$ km s^{-1} (from Fig. 13) and $R_0 = 0.5$ arcsec = 87.5 pc, we obtain a lower limit (as the radius for the cylinder can be considered a lower limit) for the mass outflow rate of ionized gas of $\dot{M} > 0.38\,\mathrm{M}_\odot\,\mathrm{yr}^{-1}$. This value is in the range of mass outflow rates observed for other Seyfert galaxies with similar luminosities (Crenshaw & Kraemer 2007; Barbosa et al. 2009; Storchi-Bergmann et al. 2010; Riffel et al. 2009; Riffel & Storchi-Bergmann 2011a), although it is much smaller than those found in recent studies for high-luminosity Seyfert 2 galaxies, with

$$\log\left(\frac{L[\mathrm{O\,III}]5007}{\mathrm{L}_\odot}\right) > 8.7,$$

which have $\dot{M}_{out} \approx 370$-$2700\,\mathrm{M}_\odot\,\mathrm{yr}^{-1}$ (e.g., McElroy et al. 2015).

Finally, due to the apparent unique velocity of the outflow, it looks like that it is not continuous, but was generated by a blast that has produced an expanding (cylindrical) shell of gas. If this is the case, we can estimate the age of the blast using $\tau = R_0/v$ resulting in $\tau = 0.8$ Myr. Actually, this can be considered an upper limit for

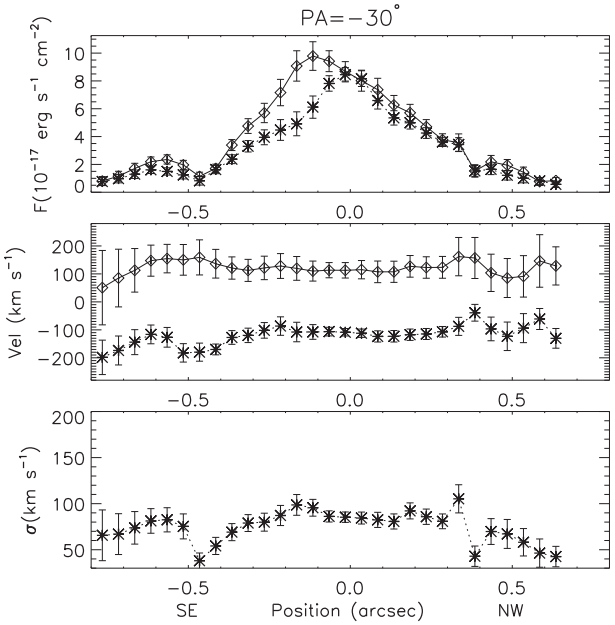

Figure 13. One-dimensional cut for the fluxes (top), velocity (middle) and velocity dispersion (bottom) from a two-Gaussian component fit to the [Fe II] emission-line profile along the SE-NW strip. The velocity dispersion was constrained to be the same for both components during the fits.

the age, as the outflow may have decelerated since the ejection from the AGN.

4.3.2 *Interaction between the radio jet and emitting gas*

Our data allowed us to observe also the kinematic effects of the interaction of the radio jet with the [Fe II] emitting gas, as discussed in Paper I based on a two-Gaussian component fit to the [Fe II] line profile. The interaction of the radio jet with the gas produces wings in the [Fe II] line profile at locations around the radio hotspots. In the single-Gaussian fit, this effect appears as an enhancement of σ at these locations, as seen in Fig. 8. Rosario et al. (2010) claims also to have found similar signatures of shocks due to the radio jet, using optical long-slit observations with the *HST*.

Although the signatures of the interaction of the radio jet with the interstellar medium (ISM) are clearly observed for the [Fe II] emission, the H_2 and H recombination lines show weaker signatures, only observed in the channel maps. This indicates that the [Fe II] emission traces a more disturbed kinematics than the molecular and atomic hydrogen. This can be interpreted as due to shocks destroying dust grains in their passage through the gas, releasing Fe atoms, which are then ionized and emit. This conclusion is supported by the reduced reddening observed along the ionization and radio jet axis of the AGN, and also in agreement with previous results we found for other Seyfert galaxies: the molecular gas and the ionized gas emitting the [Fe II] lines trace distinct kinematics and flux distributions with the former more restricted to the plane of the galaxies and the latter usually associated with outflows from the nucleus (Riffel et al. 2008, 2009, 2010a, 2013b, 2014a; Storchi-Bergmann et al. 2009, 2010; Riffel & Storchi-Bergmann 2011a; Barbosa et al. 2014).

We can also speculate on the age of the radio jet. Assuming a jet velocity of $0.1c$, if the jet were in the plane of the sky with a size of 0.5 arcsec, its age would be 2850 yr. If the inclination of the jet relative to the plane of the sky were 45°, its age would be about 4000 yr and we thus conclude that the radio jet is younger than the blast generating the equatorial outflow. Alternatively, the jet could be much more inclined towards us and could have been emitted together with the blast, taking also into consideration that the velocity of the outflow may have been larger when it was generated.

4.3.3 *Rotating disc*

As observed for the stellar velocity field, the gas velocity fields (Fig. 7) also support the presence of a rotating disc component, although the gas is clearly counter-rotating relative to the stars. This was observed by Stoklasová et al. (2009), as mentioned above. To confirm the presence of this component and derive the corresponding kinematic parameters, we fitted the Pa β, [Fe II] and H_2 velocity fields using the DISKFIT code (Spekkens & Sellwood 2007; Sellwood & Sánchez 2010; Kuzio et al. 2012) for a rotating disc model. To fit the rotation component of the gas velocity field, we excluded the velocities from the SE-NW strip. The exclusion followed the same criteria adopted in Paper I, in which regions with $\sigma > 100$ km s^{-1} for the [Fe II] line along PA $= -30/150°$ were attributed to the equatorial outflow.

The corresponding best models are shown in the centre panels of Fig. 12, while the observed velocity fields and the residual maps are presented in the left-hand and right-hand panels, respectively. As the kinematics for distinct emission lines are similar, we show only the maps for H_2 in this figure. It can be seen that the residuals are smaller than 50 km s^{-1}at most locations, indicating that the velocity fields are reasonably well represented by rotation in a disc. In Table 2, we present the kinematic parameters for the best fit models. The systemic velocity (V_s), ellipticity of the orbits (e), inclination of the disc (i) and position of the kinematical centre (X_{cen}, Y_{cen}) for the molecular gas, ionized gas and stars are very similar. The kinematical centre is measured relative to the peak of the K-band continuum and was kept fixed for the stellar velocity field to reduce the number of free parameters to be fitted, as the stellar velocity field is nosier than those of the emission lines.

The orientations of the line of nodes (Ψ_0) obtained from the fit of the gas velocity fields are consistent with each other, while Ψ_0 for the stellar velocity field is approximately opposite to that of the gas (differing by 190°).

We compare the kinematical parameters from Table 2 with those for the large-scale disc quoted in the Hyperleda data base (Paturel et al. 2003). The heliocentric systemic velocity obtained from the fit is in good agreement with the large-scale value ($V_s \approx 2503$ km s^{-1}) obtained from optical emission lines, while the inclination of the disc and the ellipticity of the orbits are a bit smaller than those for the large-scale disc [$i \approx 24°$ and $e = (1 - b/a) \approx 0.09$]. The orientation of the line of nodes is 10–20° smaller than that of the large-scale disc (e.g., Schmitt et al. 1997). We attribute the origin of this rotating gas disc to the interaction with NGC 5930. The gas velocity amplitude, corrected by the inclination of the disc is about 580 km s^{-1}. The high rotational velocities indicate that this gas is still not in orbital equilibrium in the galaxy gravitational potential. This gas is probably the source of feeding for the AGN.

4.4 Mass of ionized gas and molecular gas

The mass of the ionized gas in the inner 520 × 520 pc^2 can be estimated with

$$M_{\rm H\,II} \approx 3 \times 10^{17} \left(\frac{F_{\rm Br\,\gamma}}{[\rm erg\,s^{-1}cm^{-2}]}\right) \left(\frac{d}{[\rm Mpc]}\right)^2 [\rm M_\odot], \qquad (3)$$

where $F_{\mathrm{Br}\,\gamma}$ is the integrated flux for the Br γ emission line and d is the distance to NGC 5929 (Osterbrock & Ferland 2006; Storchi-Bergmann et al. 2009). We have assumed an electron temperature $T = 10^4$ K and electron density $N_e = 10^2\,\mathrm{cm}^{-3}$.

The mass of the warm molecular gas is given by

$$M_{\mathrm{H_2}} \approx 5.0776 \times 10^{13} \left(\frac{F_{\mathrm{H_2}\,\lambda 2.1218}}{[\mathrm{erg\,s^{-1}\,cm^{-2}}]}\right) \left(\frac{d}{[\mathrm{Mpc}]}\right)^2 \quad [\mathrm{M_\odot}], \tag{4}$$

where $F_{\mathrm{H_2}\,\lambda 2.1218}$ is the integrated flux for the H_2 λ2.1218 μm emission line and we have used the vibrational temperature $T = 2000$ K (e.g., Scoville et al. 1982; Riffel et al. 2008).

Integrating over the whole IFU field (520 × 520 pc^2) we obtain $F_{\mathrm{Br}\,\gamma} = 3.4 \pm 0.4 \times 10^{-15}\,\mathrm{erg\,s^{-1}\,cm^{-2}}$ and $F_{H_2\,\lambda 2.1218} \approx 7.3 \pm 0.9 \times 10^{-15}\,\mathrm{erg\,s^{-1}\,cm^{-2}}$, which result in $M_{\mathrm{H\,II}} = 1.3 \pm 0.2 \times 10^6\,\mathrm{M_\odot}$ and $M_{\mathrm{H_2}} = 471 \pm 58\,\mathrm{M_\odot}$.

The masses of warm molecular and ionized gas are in the range of values found for other active galaxies, which have $M_{\mathrm{H\,II}} = 10^4$–$10^7\,\mathrm{M_\odot}$ and $M_{\mathrm{H_2}} = 10^1 - 10^3\,\mathrm{M_\odot}$ (Riffel et al. 2008, 2009, 2010a,b, 2014a; Storchi-Bergmann et al. 2009; Riffel & Storchi-Bergmann 2011b; Mazzalay et al. 2013). However, the galaxies from these studies are located at a large range of distances (10–100 Mpc) and thus the corresponding sizes of the regions covered by the observations – obtained with NIFS (and SINFONI) – are distinct for the distinct objects.

To be able to compare similar quantities, we now calculate the average mass surface density, instead of the mass. For NGC 5929 we get

$$\sum_{M_{\mathrm{H_2}}} = 1.7 \times 10^{-3}\,\mathrm{M_\odot\,pc^{-2}} \text{and} \sum_{M_{\mathrm{H\,II}}} = 4.8\,\mathrm{M_\odot\,pc^{-2}}$$

for the mass surface density of the warm molecular gas and ionized gas, respectively.

These values are in the range observed for other galaxies, which range from

$$\sum_{M_{\mathrm{H_2}}} = 2.4 \times 10^{-4}\,\mathrm{M_\odot\,pc^{-2}}$$

for NGC 1068 (Riffel et al. 2014a) to

$$\sum_{M_{\mathrm{H_2}}} = 7.1 \times 10^{-3}\,\mathrm{M_\odot\,pc^{-2}}$$

for NGC 2110 (Diniz et al. 2015) for the warm molecular gas and from

$$\sum_{M_{\mathrm{H\,II}}} = 1.8 \times 10^{-1}\,\mathrm{M_\odot\,pc^{-2}}$$

for NGC 1068 (Riffel et al. 2014a) to

$$\sum_{M_{\mathrm{H\,II}}} = 42.8\,\mathrm{M_\odot\,pc^{-2}}$$

for NGC 4151 (Storchi-Bergmann et al. 2009) for the ionized gas. However, as the galaxies of our sample have distances in the range from 9.3 Mpc (for NGC 4151) to 93.8 Mpc (for Mrk 79), distinct average densities are expected for similar radial density profiles with decreasing gas densities as a function of distance from the nucleus.

To compare the mass of ionized gas and warm molecular gas closest to the nucleus, we used the previous data obtained by our group to estimate the mass within a fixed physical aperture of 100 × 100 pc^2. This aperture was chosen as being the whole field of view of the nearest object of the sample. The mass of ionized gas within this aperture is in the range 0.3–27 × 10^5 $\mathrm{M_\odot}$ and the mass of warm molecular gas ranges from 3 to 455 $\mathrm{M_\odot}$, approximately. The lowest masses for both ionized gas and molecular gas are observed for NGC 4051, while NGC 1068 has the highest values. For NGC 5929 we find $M_{\mathrm{H\,II}} = 3 \pm 0.5 \times 10^5\,\mathrm{M_\odot}$ and $M_{\mathrm{H_2}} = 47 \pm 6\,\mathrm{M_\odot}$ for the inner 100 × 100 pc^2, which corresponds to an aperture of only 0.6 arcsec × 0.6 arcsec. The median ratio between the masses of ionized gas and molecular gas is 6.9 × 10^3, similar to the ratio for NGC 5929 of ∼6.4 × 10^3.

However, the total mass of molecular gas, including cold gas, is much larger than the values obtained here. The ratio between cold gas and warm molecular gas observed in the central region of active galaxies is in the range 10^5–10^7 (Dale et al. 2005; Müller-Sánchez et al. 2006; Mazzalay et al. 2013) and thus, the total amount of molecular gas in the inner 3 arcsec × 3 arcsec of NGC 5929 should be at least 4.7 × $10^7\,\mathrm{M_\odot}$ with a surface mass density of $170\,\mathrm{M_\odot\,pc^{-2}}$.

4.5 The origin of the [Fe II] emission

The origin of the [Fe II] emission in AGNs can be investigated using the line-ratio maps shown in Fig. 4. The [Fe II] emission is excited in partially ionized-gas regions, which can be produced by X-rays (e.g., Simpson et al. 1996) and/or shock heating (e.g., Forbes & Ward 1993) of the gas. Values of [Fe II]/Pa β >2.0 indicate that most of the [Fe II] line emission is produced by shocks, while [Fe II]/Pa β <0.6 indicate that photoionization dominates the emission (Rodríguez-Ardila et al. 2004; Rodríguez-Ardila, Riffel & Pastoriza 2005).

The [Fe II] λ1.2570μm/Pa β line ratio for NGC 5929 is shown in the top-right panel of Fig. 4. At most positions, this ratio has values larger than 0.6, with the exception of only a small region at ∼0.8 arcsec north-north-east of the nucleus. At locations co-spatial with the radio knots, the [Fe II] λ1.2570μm/Pa β ratio is larger than 2.0, suggesting that the interaction of the radio jet with the gas has an important role in the observed [Fe II] emission. At the north-eastern radio hotspot, [Fe II]/Pa β ≈2.3, while at the south-western radio hotspot [Fe II]/Pa β ≈2.8. At the nucleus and along the SE-NW strip a typical value for [Fe II]/Pa β is 1.5, suggesting that both photoionization and shocks contribute to the excitation of [Fe II], with a larger contribution from shocks though (as this value is closer to 2.0 than to 0.6).

The [Fe II] λ1.2570 μm and [P II] λ1.8861 μm lines have similar excitation temperatures, and their parent ions have similar ionization potentials and radiative recombination coefficients. The [Fe II]/[P II] line-ratio map shown in the top-left panel of Fig. 4 is useful for investigating the origin of [Fe II] emission. Values larger than 2.0 indicate that shocks have passed through the gas destroying the dust grains, releasing the Fe and thus enhancing its observed abundance. For supernova remnants, where shocks are the dominant excitation mechanism, [Fe II]/[P II] is typically higher than 20 (Oliva et al. 2001). In NGC 5929, at all locations where both lines are detected, [Fe II]/[P II] is larger than 2.0, suggesting that shocks contribute to the [Fe II] emission and supporting the conclusion from the [Fe II]/Pa β ratio map. At the position of the hotspots, values of up to 10 are observed, supporting an even stronger interaction with the radio jet and with the gas.

As the [Fe II] emission-line profiles are complex at many locations, as seen in Fig. 2, with extended wings at locations close to the radio knots and double components along the SE-NW strip, we also constructed [Fe II]/Pa β line-ratio channel maps (constructing

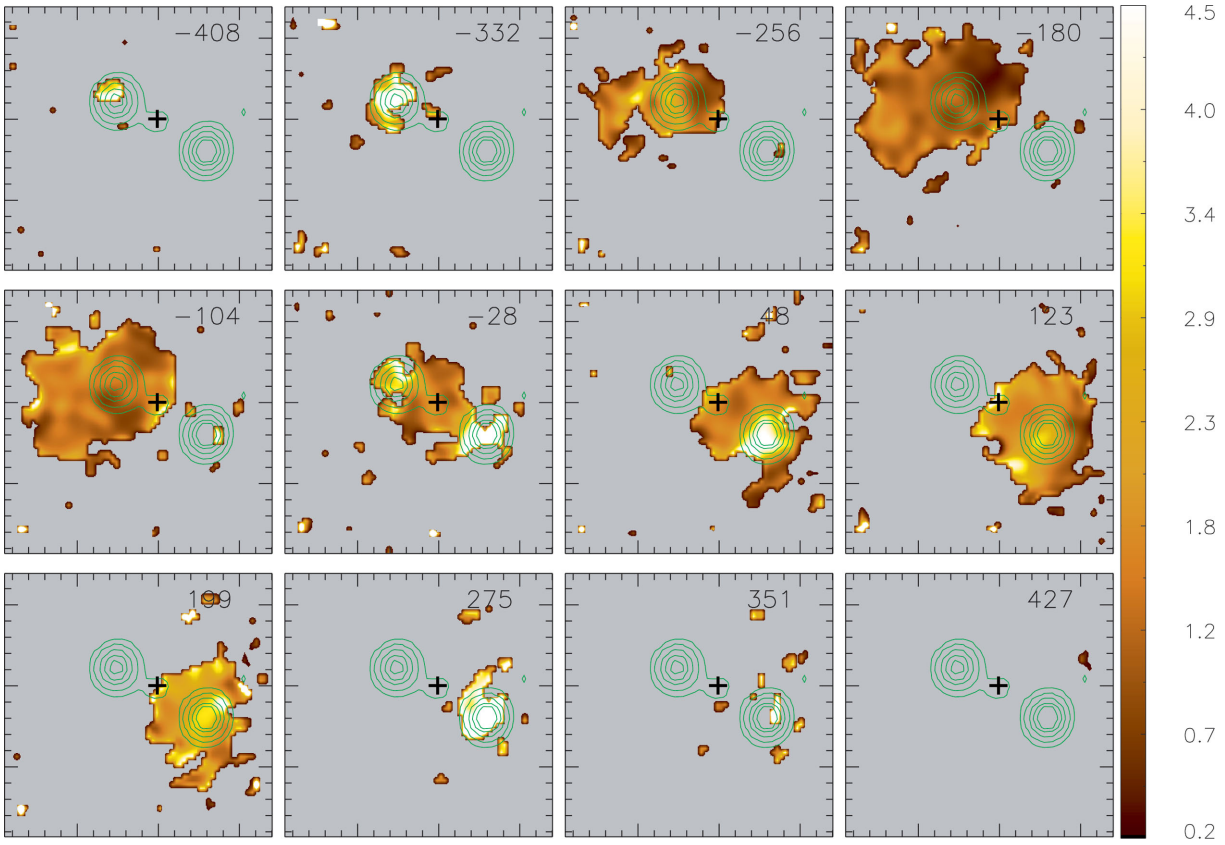

Figure 14. Velocity channel maps for the [Fe II] λ1.2570 μm/Pa β line ratio. Each panel shows the fluxes centred at the velocity shown in the top-right corner relative to the systemic velocity of the galaxy. Grey regions are locations where one or both lines have fluxes smaller that 3σ (the standard deviation of the continuum next to the line) and the green contours are from the radio image of Ulvestad & Wilson (1989).

line ratios at different velocity bins) to determine the gas excitation mechanism at distinct velocities. The resulting channel maps are shown in Fig. 14. Each panel presents the [Fe II]/Pa β line-ratio map centred at the velocity shown in the top-right corner of the panel, relative to the systemic velocity of the galaxy. To avoid spurious features, we masked regions in which one or both lines have fluxes smaller than three times the standard deviation of the continuum next to the line. These regions are shown in grey in the figure. The contours are from the radio image.

The [Fe II]/Pa β ratio has values ranging from 0.2 up to 4.5. The highest values are observed for the gas at the highest velocities (largest blue shifts and red shifts) and present an excellent correlation with the radio knots. These high [Fe II]/Pa β values are interpreted as strong evidence that the [Fe II] is produced by the interaction of the radio jet with the NLR gas. For smaller velocities, at most locations the values are smaller than 2.0, with typical values of ∼1.2, suggesting that X-rays from the central AGN are the main drivers of the [Fe II] emission. Line emission is observed along the SE-NW strip only at velocities lower than 180 km s^{-1}. The values of [Fe II]/Pa β there are somewhat higher than observed at other locations, but still much smaller than those seen at the radio knots. Typical values are [Fe II]/Pa β =2–3, suggesting that shocks are also important along the SE-NW strip. These shocks may be associated with the equatorial outflows we reported at these locations in Paper I.

We conclude that the main excitation mechanism of the [Fe II] emission in NGC 5929 is shocks due to the radio jet, with some contribution from X-ray heating at locations distant from the radio structures. The highest-velocity gas is associated with the interaction of the radio jet with the ISM and thus we conclude that its [Fe II] emission is produced mainly by shocks, while X-ray excitation is more important for the rotating gas at lower velocities. These results are supported by the line-ratio maps and by the correlation between the emission-line flux distributions and the radio image, and are in good agreement with those of previous similar studies for other Seyfert galaxies (e.g., Rodríguez-Ardila et al. 2004, 2005; Storchi-Bergmann et al. 1999, 2009; Riffel et al. 2006, 2010a).

4.6 H_2 excitation

The excitation of the H_2 line emission in the near-IR can be due to fluorescence through absorption of soft-UV photons (912–1108 Å) in the Lyman and Werner bands (Black & van Dishoeck 1987) and/or by thermal processes due to the heating of the gas by shocks (due to the interaction of the radio jet with the emitting gas and/or supernovae) (Hollenbach & McKee 1989) or by X-rays from the central AGN (Maloney, Hollenbach & Tielens 1996). Several works have studied the origin of the H_2 emission in AGNs using long-slit spectroscopy (e.g., Reunanen, Kotilainen & Prieto 2002; Rodríguez-Ardila et al. 2004, 2005; Davies et al. 2005; Ramos Almeida, Pérez García & Acosta-Pulido 2009) and integral-field spectroscopy (e.g., Riffel et al. 2006, 2008, 2010a,b, 2014a; Storchi-Bergmann et al. 2009; Riffel & Storchi-Bergmann 2011b; Müller-Sánchez et al. 2009; Hicks et al. 2009; Friedrich et al. 2010; Mazzalay et al. 2013; Iserlohe et al. 2013).

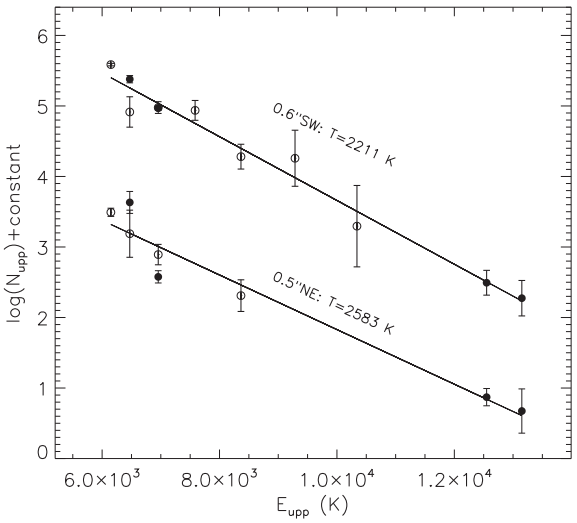

Figure 15. Relation between $N_{\rm upp} = F_i\lambda_i/A_i g_i$ and $E_{\rm upp} = T_i$ for the H_2 emission lines for thermal excitation at the locations of the radio hotspots. Ortho (S) transitions are shown as filled circles and para (Q) transitions as open circles.

To distinguish between fluorescence and thermal processes, we used the observed fluxes for all H_2 emission lines in the K band to calculate the thermal excitation temperature. If the H_2 emission is dominated by thermal processes and under the assumption of an ortho:para abundance ratio of 3: 1, the following relation is valid (Wilman, Edge & Juhnstone 2005):

$$\log\left(\frac{F_i\lambda_i}{A_i g_i}\right) = \text{constant} - \frac{T_i}{T_{\rm exc}}, \quad (5)$$

where F_i is the flux of the ith H_2 line, λ_i is its wavelength, A_i is the spontaneous emission coefficient, g_i is the statistical weight of the upper level of the transition, T_i is the energy of the level expressed as a temperature and $T_{\rm exc}$ is the excitation temperature. Thus, if the observed fluxes can be reproduced by the equation above, H_2 emission may be dominated by thermal processes. The resulting plot for $N_{\rm upp} = F_i\lambda_i/A_i g_i$ (plus an arbitrary constant) versus $E_{\rm upp} = T_i$ is shown in Fig. 15 for the fluxes shown in Table 1 for the locations of the two radio hotspots at 0.5 arcsec north-east and 0.6 arcsec south-west of the nucleus. We do not show plots for other positions of Table 1 because only a few H_2 lines were detected at these locations. As seen in Fig. 15, the observed fluxes are well reproduced by the equation (shown as a continuum line) at both positions, indicating that thermal processes are the main excitation mechanism of the H_2 lines. The resulting excitation temperatures are $T_{\rm exc} = 2583 \pm 40$ K and $T_{\rm exc} = 2211 \pm 37$ K at 0.5 arcsec north-east and 0.6 arcsec south-west of the nucleus, respectively.

The H_2 λ2.1218/Br γ emission-line-ratio map shown in Fig. 4 can also be used to investigate the nature of H_2 excitation. For starburst galaxies and H II regions, this ratio is H_2/Br γ < 0.6. Larger values are observed for Seyfert nuclei, where the heating of the gas by shocks and X-rays provides additional thermal excitation. Typical values for Seyfert galaxies are in the range $0.6 <$ H_2 λ2.1218/Br γ < 2.0 (Rodríguez-Ardila et al. 2004, 2005), although recent studies suggest a broader range of values $0.4 <$ H_2 λ2.1218/Br γ < 6.0 for AGNs, including LINERs (Riffel et al. 2013a). NGC 5929 has values larger than 2.0 at most locations, confirming that thermal processes dominate the H_2 excitation. The only exception is a small region with values of ∼0.3 at ∼0.8 arcsec north-north-east of the nucleus, where [Fe II]/Pa β also has small values. Typical values to the north-east are H_2/Br γ ≈1.0, while to the south-west values of up to 4.5 are observed in regions surrounding the radio knot, suggesting that shocks due to the radio jet contribute to the H_2 emission at this location. Similar high values are also observed at the nucleus and along the SE-NW strip, where the interaction of the outflows seen in Paper I with the ambient gas might enhance the H_2 emission.

We also constructed channel maps for the H_2/Br γ ratio to investigate the origin of the H_2 emission at distinct kinematics. These channel maps are shown in Fig. 16. The range of velocities is much smaller than those seen for the [Fe II]/Pa β channel maps in Fig. 14 and the maps are much noisier due to a lower S/N ratio for the K-band lines. At locations of the radio knots, the H_2/Br γ values are larger than 2.0, supporting the contribution to the H_2 excitation of shocks due to the radio jet at these positions, in particular at the south-western radio knot, where the highest values of H_2/Br γ are observed in the channel maps for the highest velocities.

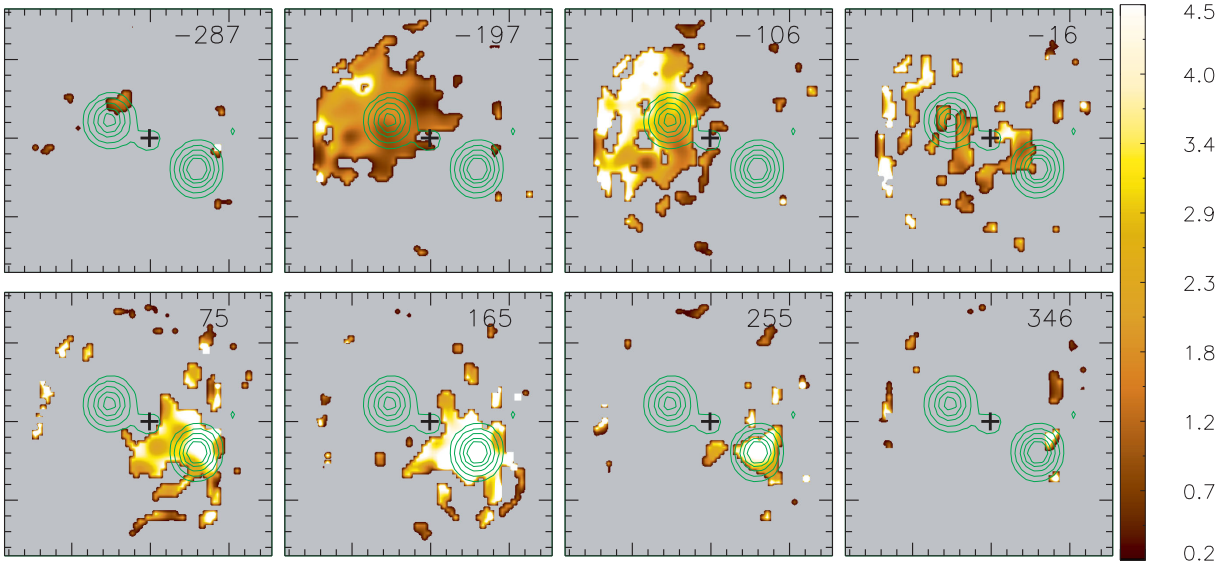

Figure 16. Same as Fig. 14 for the H_2 λ2.1218/Br γ line ratio.

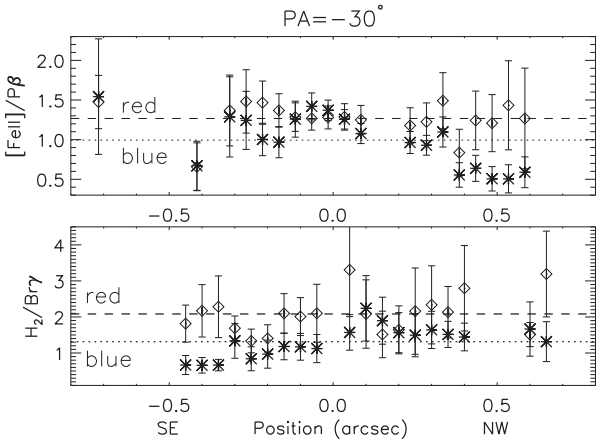

Figure 17. [Fe II]/Pa β and H_2/Br γ emission-line ratios along PA $= -30/150°$. The red component is shown as open diamonds and the blue component as asterisks. The dashed line shows the average value for the red component and the dotted line represents the average ratio for the blue component.

Finally, H_2 λ2.2477/λ2.1218 can also be used to distinguish between excitation of H_2 by thermal processes and fluorescence. For thermal processes, this ratio is ∼0.1–0.2 and for fluorescent excitation it is ∼0.55 (e.g., Mouri 1994; Reunanen et al. 2002; Rodríguez-Ardila et al. 2004; Storchi-Bergmann et al. 2009). The H_2 λ2.2477/λ2.1218 ratio map is shown in Fig. 4 and has values ranging from 0.1 to 0.25, supporting the conclusion above that fluorescent excitation is not important for NGC 5929.

Thus, we conclude that the H_2 emission observed in NGC 5929 is excited by thermal processes, due to heating of the gas by shocks and X-rays from the central AGN. At locations co-spatial with the radio jet and along the SE-NW strip, shocks play an important role as indicated by the enhancement of the line ratios. Away from these locations, X-ray heating may dominate the H_2 excitation.

4.7 The origin of the double components

Do the double components observed along the SE-NW strip have a distinct origin unlike the emission from the disc? We can better investigate the origin of the emission of the outflowing gas using the emission-line ratios. Fig. 17 presents the [Fe II]/Pa β and H_2/Br γ emission-line ratios for the blue (asterisks) and red (diamonds) components along a pseudo slit with 0.35 arcsec width oriented along the SE-NW strip at PA $= -30/150°$. For [Fe II]/Pa β, both components have values typical of Seyfert galaxies, with average values of 1.0 and 1.3 for the blue and red components, respectively. H_2/Br γ has some values larger than 2 at some positions, but at most locations this ratio has values typical of Seyfert galaxies. The average values are 1.3 and 2.1 for the blue and red components, respectively. As the line ratio of both components has values typical of Seyfert galaxies, the emission of the outflowing gas might be due to heating by X-rays from the central AGN.

5 CONCLUSIONS

We used Gemini integral field J- and K_1-band spectroscopy of the inner 250 pc radius of the Seyfert 2 galaxy NGC 5929, at spatial resolution 20 pc and velocity resolution 40 km s^{-1}, to map the stellar and gas kinematics and the flux distributions of emission lines from the ionized gas and warm molecular gas. Our main conclusions are:

(i) The flux distributions for the H_2, H recombination and forbidden emission lines are extended up to 250 pc, with the highest flux levels oriented along PA $= 60/240°$ (the direction of the radio jet), and they are well correlated with the radio emission. The H_2 emission is more distributed over the whole field of view, while the emission of the ionized gas is more collimated along the direction of the radio jet.

(ii) The excitation of H_2 and [Fe II] at all locations is dominated by thermal processes, mainly due to heating of the gas by X-rays emitted by the central AGN. Some contribution from shocks is observed in the high-velocity gas at locations next to the radio hotspots, as indicated by the [Fe II]/Pa β and H_2/Br γ line-ratio channel maps.

(iii) The stellar velocity field shows rotation with an amplitude up to ∼200 km s^{-1} when corrected for the inferred inclination of 18.3°, and a velocity dispersion reaching 180 km s^{-1}. From the $M_\bullet$–σ relation, we estimated a mass for the supermassive black hole of $M_\bullet = 5.2^{1.6}_{-1.2} \times 10^7\,M_\odot$ using the median stellar velocity dispersion of $\sigma_* = 133 \pm 8$ km s^{-1}.

(iv) The gas kinematics has three components: (1) a counter-rotating disc (relative to the stellar velocity field); (2) an equatorial outflow (perpendicular to the radio jet), thus in the plane of the torus, with a mass outflow rate of $\dot{M} > 0.4\,M_\odot\,yr^{-1}$ and (3) kinematic disturbances observed in association with the radio hotspots in blue shift to the north-east and red shift to the south-west, which supports that the radio jet is tilted towards us at the north-east and away from us at the south-west.

(v) From the Br γ and H_2 emission-line fluxes, we calculate the masses of ionized gas and warm molecular gas as

$$M_{H\,II} = 1.3 \pm 0.2 \times 10^6\,M_\odot \quad \text{and} \quad M_{H_2} = 471 \pm 58\,M_\odot,$$

respectively. These values correspond to mass surface densities of

$$\sum_{M_{H_2}} = 1.7 \times 10^{-3}\,M_\odot\,pc^{-2} \quad \text{and} \quad \sum_{M_{H\,II}} = 4.8\,M_\odot\,pc^{-2},$$

which are in the range of values observed for other galaxies.

Our favoured scenario for this galaxy is that the interaction with NGC 5930 has sent gas towards the nucleus of NGC 5929, triggering the nuclear activity. If the observed equatorial outflow can be considered the first blast of the AGN, we estimate that this happened less than 1 Myr ago.

ACKNOWLEDGEMENTS

We thank the referee for his/her thorough review, comments and suggestions, which helped us to improve this paper significantly. This research was based on observations obtained at the Gemini Observatory, which is operated by the Association of Universities for Research in Astronomy, Inc, under a cooperative agreement with the National Science Foundation on behalf of the Gemini partnership: the National Science Foundation (United States), the Science and Technology Facilities Council (United Kingdom), the National Research Council (Canada), CONICYT (Chile), the Australian Research Council (Australia), Ministério da Ciência e Tecnologia (Brazil) and SECYT (Argentina). This research made use of the NASA/IPAC Extragalactic Database (NED), which is operated by the Jet Propulsion Laboratory, California Institute of Technology, under contract with the National Aeronautics and Space Administration. RAR acknowledges support from FAPERGS (project 2366-2551/14-0) and CNPq (projects 470090/2013-8 and 302683/2013-5).

REFERENCES

Baillard A. et al., 2011, A&A, 532, 74
Barbosa F. K. B., Storchi-Bergmann T., Cid Fernandes R., Winge C., Schmitt H., 2009, MNRAS, 396, 2
Barbosa F. K., Storchi-Bergmann, McGregor P., Vale T. B., Riffel R. A., 2014, MNRAS, 455, 2353
Black J. H., van Dishoeck E. F., 1987, ApJ, 322, 412
Cappellari M., Emsellem E., 2004, PASP, 116, 138
CardelliJ. A., Clayton G. C., Mathis J. S., 1989, ApJ, 345, 245
Crenshaw D. M., Kraemer S. B., 2007, ApJ, 659, 250
Dale D. A., Sheth K., Helou G., Regan M. W., Hüttemeister S., 2005, ApJ, 129, 2197
Davies R. I. I., Sternberg A., Lehnert M. D., Tacconi-Garman L. E., 2005, ApJ, 633, 105
Davies R. I., Maciejewski W., Hicks E. K. S., Tacconi L. J., Genzel R., Engel H., 2009, ApJ, 702, 114
Davies R. I. et al., 2014, ApJ, 792, 101
Diniz M. R., Riffel R. A., Stochi-Bergmann T., Winge C., 2015, MNRAS, submitted
Elitzur M., 2012, ApJ, 747, L33
Fathi K., Storchi-Bergmann T., Riffel R. A., Winge C., Axon D. J., Robinson A., Capetti A., Marconi A., 2006, ApJ, 641, L25
Ferruit P., Pecontal E., Wilson A. S., Binette L., Wilson A. S., 1997, A&A, 328, 493
Ferruit P., Wilson A. S., Whittle M., Simpson C., Mulchaey J. S., Ferland G., 1999, ApJ, 523, 147
Forbes D. A., Ward M. J., 1993, ApJ, 416, 150
Friedrich S., Davies R. I., Hicks E. K. S., Engel H., Müller-Sánchez F., Genzel R., Tacconi L. J., 2010, A&A, 519, 79
Graham A. W., Scott N., 2013, ApJ, 764, 151
Hicks E. K. S., Davies R. I., Malkan M. A., Genzel R., Tacconi L. J., Sánchez F. M., Sternberg A., 2009, ApJ, 696, 448
Hicks E. K. S., Davies R. I., Maciejewski W., Emsellem E., Malkan M. A., Dumas G., Müller-Sánchez F., Rivers A., 2013, ApJ, 768, 107
Hollenbach D., McKee C. F., 1989, ApJ, 342, 306
Hönig S. F. et al., 2013, MNRAS, 771, 87
Iserlohe C., Krabbe A., Larkin J. E., Barczys M., McElwain M. W., Quirrenbach A., Weiss J., Wright S. A., 2013, A&A, 556, 136
Keel W. C., 1985, Nature, 318, 43
Kormendy J., Ho L. C., 2013, ARA&A, 51, 511
Kuzio de Naray R., Arsenault C. A., Spekkens K., Sellwood J. A., McDonald M., Simon J. D., Teuben P., 2012, MNRAS, 427, 2523
Li J., Ostriker J., Sunyaev R., 2013, ApJ, 767, L105
Malkan M. A., Gorjian V., Tam R., 1998, ApJS, 117, 25
Maloney P. R., Hollenbach D. J., Tielens A. G. G. M., 1996, ApJ, 466, 561
Mazzalay X. et al., 2013, MNRAS, 428, 2389
Mazzalay X. et al., 2014, MNRAS, 438, 2036
McElroy R., Croom S. M., Pracy M., Sharp R., Ho I.-T., Medling A. M., 2015, MNRAS, 446, 2186
McGregor P. J. et al., 2003, Proc. SPIE, 4841, 1581
Mouri H., 1994, ApJ, 427, 777
Müller-Sánchez F., Davies R. I., Eisenhauer F., Tacconi L. J., Genzel R., Sternberg A., 2006, A&A, 454, 492
Müller-Sánchez F., Davies R. I., Genzel R., Tacconi L. J., Eisenhauer F., Hicks E. K. S., Friedrich S., Sternberg A., 2009, ApJ, 691, 749
Oliva E. et al., 2001, A&A, 369, L5
Osterbrock D. E., Ferland G. J., 2006, Astrophysics of Gaseous Nebulae and Active Galactic Nuclei, 2nd edn. University Science Books, Mill Valley, California
Page T., 1952, ApJ, 116, 63
Paturel G., Petit C., Prugniel Ph., Theureau G., Rousseau J., Brouty M., Dubois P., Cambrésy L., 2003, A&A, 412, 45
Ramos Almeida C., Pérez García A. M., Acosta-Pulido J. A., 2009, ApJ, 694, 1379
Reunanen J., Kotilainen J. K., Prieto M. A., 2002, MNRAS, 331, 154
Riffel R. A., 2010, Ap&SS, 327, 239
Riffel R. A., Sorchi-Bergmann T., Winge C., Barbosa F. K. B., 2006, MNRAS, 373, 2
Riffel R. A., Storchi-Bergmann T., Winge C., McGregor P., Beck T., Schmitt H., 2008, MNRAS, 385, 1129
Riffel R. A., Storchi-Bergmann T., Dors O. L., Winge C., 2009, MNRAS, 393, 783
Riffel R. A., Storchi-Bergmann T., Nagar N. M., 2010a, MNRAS, 404, 166
Riffel R. A. Storchi-Bergmann T., Riffel R., Pastoriza M. G., 2010b, ApJ, 713, 469
Riffel R. A. Storchi-Bergmann T., 2011a, MNRAS, 411, 469
Riffel R. A. Storchi-Bergmann T., 2011b, MNRAS, 417, 2752
Riffel R., Riffel R. A., Ferrari F., Storchi-Bergmann T., 2011c, MNRAS, 416, 493
Riffel R., Rodríguez-Ardila A., Aleman I., Brotherton M. S., Pastoriza M. G., Bonatto C., Dors O. L., 2013a, MNRAS, 430, 2002
Riffel R. A., Storchi-Bergmann T., Winge C., 2013b, MNRAS, 430, 2249
Riffel R. A., Storchi-Bergmann, Vale T. B., McGregor P., 2014a, MNRAS, 442, 656
Riffel R. A., Storchi-Bergmann T., Riffel R., 2014b, ApJ, 780, L24 (Paper I)
Rodríguez-Ardila A., Pastoriza M. G., Viegas S., Sigut T. A. A., Pradhan A. K., 2004, A&A, 425, 457
Rodríguez-Ardila A., Riffel R., Pastoriza M. G., 2005, MNRAS, 364, 1041
Rosario D. J., Whittle M., Nelson C. H., Wilson A. S., 2010, ApJ, 711, L94
Schartmann M., Burkert A., Krause M., Camenzind M., Meisenheimer K., Davies R. I., 2010, MNRAS, 403, 1801
Schmitt H. R., Kinney A. L., Storchi-Bergmann T., Antonucci R., 1997, ApJ, 477, 623
Schnorr-Müller A., Storchi-Bergmann T., Riffel R. A., Ferrari F., Steiner J. E., Axon D. J., Robinson A., 2011, MNRAS, 413, 149
Schnorr-Müller A., Storchi-Bergmann T., Nagar N. M., Lena D., Riffel R. A., Couto G. S., 2014a, MNRAS, 438, 3322
Schnorr-Müller A., Storchi-Bergmann T., Nagar N. M., Robinson A., Ferrari F., 2014b, MNRAS, 437, 1708
Schönel A. J., Jr, Riffel R. A., Stochi-Bergmann T., Winge C., 2014, MNRAS, 445, 4014
Scoville N. Z., Hall D. N. B., Kleinmann S. G., Ridgway S. T., 1982, ApJ, 253, 136
Sellwood J. A., Sáanchez R. Z., 2010, MNRAS, 404, 1733
Simpson C., Forbes D. A., Baker A. C., Ward M. J., 1996, MNRAS, 283, 777
Spekkens K., Sellwood J. A., 2007, ApJ, 664, 204
Stoklasová I., Ferruit P., Emsellem E., Jungwiert B., Pécontal E., Sánchez S. F., 2009, A&A, 500, 1287
Storchi-Bergmann T., 2013, BrJPh, 43, 383
Storchi-Bergmann T., 2014, in Ziegler B. L., Combes F., Dannerbauer H., Verdugo M., eds, Proc. IAU Symp. 309, Galaxies in 3D across the Universe. Cambridge Univ. Press, Cambridge
Storchi-Bergmann T., Winge C., Ward M. J., Wilson A. S., 1999, MNRAS, 304, 35
Storchi-Bergmann T., Dors O., Jr Riffel R. A., Fathi K., Axon D. J., Robinson A., 2007, ApJ, 670, 959
Storchi-Bergmann T., McGregor P., Riffel R. A., Simões Lopes R., Beck T., Dopita M., 2009, MNRAS, 394, 1148
Storchi-Bergmann T., Simões Lopes R., McGregor P., Riffel R. A., Beck T., Martini P., 2010, MNRAS, 402, 819
Storchi-Bergmann T., Riffel R. A., Riffel R., Diniz M. R., Borges Vale T., McGregor P. J., 2012, ApJ, 755, 87
Su B. M., Muxlow T. W. B., Pedlar A., Holloway A. J., Steffen W., Kukula M. J., Mutel R. L., 1996, MNRAS, 279, 1111
Ulvestad J. S., Wilson A. S., 1984, ApJ, 285, 439
Ulvestad J. S., Wilson A. S., 1989, ApJ, 343, 659
Whittle M., Haniff C. A., Ward M. J., Meurs E. J. A., Pedlar A., Unger S. W., Axon D. J., Harrison B. A., 1986, MNRAS, 222, 189
Wilman R. J., Edge A. C., Juhnstone R. M., 2005, MNRAS, 359, 755
Wilson A. S., Keel W. C., 1989, AJ, 98, 1581
Winge C., Riffel R. A., Storchi-Bergmann T., 2009, ApJS, 185, 186

This paper has been typeset from a TEX/LATEX file prepared by the author.